Petroleum Science 23 (2026) 496–513

Contents lists available at ScienceDirect

Petroleum Science

journal homepage: www.keaipublishing.com/en/journals/petroleum-science

Original Paper

Synthesis of biopolymer nanocomposites and experimental investigation on enhanced oil recovery

Bo Wang [a], Shu-Yuan Deng [a], Hao Zeng [b], Feng-Peng Lai [a], Qing Feng [c], Xiao-Nan Li [c], Yue-Hui She [d,e,f,**], Fan Zhang [a,*]

[a] School of Energy Resources, China University of Geosciences (Beijing), Beijing, 100083, China
[b] Jianghan Oil Production Plant, Sinopec Jianghan Oilfield Company, Qianjiang, 433123, Hubei, China
[c] Oilfield Production Optimization Institution of China National Offshore Oil Corporation, Tianjin, 300459, China
[d] College of Petroleum Engineering, Yangtze University, Wuhan, 430100, Hubei, China
[e] State Key Laboratory of Low Carbon Catalysis and Carbon Dioxide Utilization, Wuhan, 430100, Hubei, China
[f] Cooperative Innovation Center of Unconventional Oil and Gas, Wuhan, 430100, Hubei, China

ARTICLE INFO

Article history:
Received 26 February 2025
Received in revised form
17 May 2025
Accepted 11 August 2025
Available online 19 August 2025

Edited by Min Li

Keywords:
Biosynthesis
Nanoparticles
Biopolymer nanocomposites
Dispersion stability
Enhanced oil recovery

ABSTRACT

Nanoparticles (NPs) are widely used in the petroleum industry, particularly in upstream and downstream applications, due to their quantum effects and high surface area-to-volume ratio. However, stable dispersion and high input ratios of NPs are critical factors limiting their application. This study thus synthesizes the biopolymer nanocomposite E-Ag NPs in one step using the metabolic product exopolysaccharide (EPS) from *Bacillus subtilis* as both a reducing and stabilizing agent. This study explored the potential of E-Ag NPs to enhance oil recovery in low- and medium-permeability formations. Experimental results showed that the average particle size of Ag NPs synthesized using EPS ranged from 20 to 50 nm. The presence of EPS resulted in a higher Zeta potential value (−43.4 mV), indicating improved stability of the nanofluid, effectively inhibiting NPs aggregation. Interfacial tension and wettability evaluation experiments demonstrated that E-Ag NPs exhibited excellent capabilities in reducing interfacial tension and altering wettability. In the enhanced oil recovery evaluation experiments, the imbibition experiment with E-Ag NPs achieved a maximum recovery rate of 54.32%, and the core flooding experiment reached a maximum recovery rate of 16.33%. In conclusion, the biopolymer nanocomposites developed by this method offer valuable guidance and reference for oilfield development, providing a green and efficient potential solution for enhanced oil recovery.

1. Introduction

As a strategically significant non-renewable energy source, petroleum has undergone decades of exploration, development, and extraction (Suleiman, 2019). Currently, oil fields worldwide are entering a period of decline, with less than 50% of the crude oil being recoverable through primary and secondary recovery methods (Iravani et al., 2023). Therefore, adopting more efficient methods to enhance oil recovery (EOR) has garnered widespread attention from researchers in the industry. In recent years, the use of nanotechnology to improve the efficiency of crude oil extraction has become a mainstream research direction in the petroleum industry (Aziz and Tunio, 2019; Rezk and Allam, 2019; Sun et al., 2020). Nanotechnology involves the use of nanoparticles (ranging in size from 1 to 100 nm) and their suspensions to enhance oil recovery (Esfe et al., 2020). NPs possess properties such as high specific surface area, chemical reactivity, and chemo catalysis (Bera and Belhaj, 2016; Kazemzadeh et al., 2018), making them widely applicable in environmental protection, petroleum extraction, and pharmaceutical products (Morones et al., 2005).

In oil reservoirs, NPs are widely used for enhancing crude oil recovery in porous media due to their small size, which allows easy movement through the porous media of reservoir rocks

* Corresponding author.
** Corresponding author.
E-mail addresses: sheyuehui@163.com (Y.-H. She), fanzhang@cugb.edu.cn (F. Zhang).
Peer review under the responsibility of China University of Petroleum (Beijing).

https://doi.org/10.1016/j.petsci.2025.08.020

(Bahraminejad et al., 2019; Kazemzadeh et al., 2019; Rezvani et al., 2018; Suleimanov et al., 2023). Their ability to alter fluid properties and increase the stability of fluids, such as polymers and surfactants (Maurya and Mandal, 2018), along with their higher temperature and pressure resistance and compatibility compared to other materials (Maurya et al., 2017; Nassar et al., 2011). For example, Liu et al. (2023) investigated the application of metallic silver nanofluids prepared using the biophilic reducing agent ascorbic acid for EOR. They found that the silver nanofluids could be adsorbed onto the walls of the porous media and strip residual oil, resulting in a residual oil recovery of up to 19.49%. NPs primarily achieve efficient oil recovery by reducing interfacial tension (IFT) (Agi et al., 2020b; Betancur et al., 2019), altering reservoir rock wettability (Al-Anssari et al., 2016; Wang et al., 2024), increasing the viscosity (Ali et al., 2019; Sharma et al., 2015) and rheology of injected fluids (Agi et al., 2020a; Wei et al., 2018), and inhibiting asphaltene precipitation. These mechanisms make nanomaterials exhibit superior performance compared to conventional chemical oil displacement agents. However, the stable dispersion of NPs, high input ratios, and poor compatibility with other materials remain significant factors limiting their application in enhanced recovery. Therefore, reducing the manufacturing cost of NPs, improving their compatibility with other oil displacement agents, and enhancing their stable dispersion in the system are the current research focus (Druetta and Picchioni, 2019; Dzhardimalieva et al., 2021; Emadi et al., 2017; Sofla et al., 2018; Sun et al., 2020).

Currently, the synthesis methods of NPs mainly include chemical, physical, and biological approaches. Chemical and physical methods produce a large amount of toxic chemical pollutants during NPs synthesis, have long synthesis times, and consume significant amounts of energy, which can cause irreversible environmental damage (Ahmed et al., 2016; Saravanan et al., 2021). Biological methods, on the other hand, offer advantages such as biocompatibility, low production cost, short synthesis time, high yield, and natural reduction (Hoseinzadeh et al., 2017). Additionally, the synthesized NPs can self-stabilize and disperse in bioactive substances without the need for an additional capping or attachment step (Gahlawat and Choudhury, 2019). For example, Arsiya et al. (2017) were able to biosynthesize Pd NPs within 10 min at room temperature using chlorella vulgaris. Fourier transform infrared spectroscopy (FTIR) analysis showed the presence of polyol and amide groups in the extract, which acted as reducing and stabilizing agents during the synthesis. The biosynthesis of NPs primarily utilizes bacteria, fungi, plant extracts, or biopolymers as reducing agents to convert metal ions via electron transfer. Concurrently, biosurfactants, biopolymers, and other macromolecules present in the system function as capping agents that restrict metal nucleation to nanoscale dimensions, thereby stabilizing the formed NPs (Malhotra and Alghuthaymi, 2022).

Biopolymers, as sustainable and renewable natural materials, are synthesized by microorganisms such as algal plants, bacteria, and fungi. They offer advantages such as easy production processes, high growth rates, non-toxicity, high compatibility, and environmental friendliness (Bajestani et al., 2017; Riaz et al., 2021). Due to their unique long-chain and helical structures, biocompatibility, biodegradability, and production sustainability, they are widely used in the synthesis and stabilization of nanomaterials. Biopolymers are used to synthesize NPs by dispersing metal cations in a polymer network via the “polymer complexation method” and utilizing aldehyde or carboxylic acid groups in the biopolymer to reduce the metal ions in situ (Schnepp, 2013). Additionally, biopolymers are highly efficient oil displacement agents (Abbaspour et al., 2023), exhibiting excellent rheological properties and efficiency in harsh formation environments. Therefore, the presence of biopolymers enhances the recovery effect of NPs, and the combination of the two has a positive synergistic effect in the EOR process.

In this work, a novel biopolymer-based nanocomposite material (E-Ag NPs) was synthesized in a one-step process by in situ reduction of Ag^+ using the biopolymer EPS, a metabolite of *Bacillus subtilis*, as both a reducing and stabilizing agent (Becker et al., 2009; Emam and Ahmed, 2016). To the best of our knowledge, there are few reports on the application of environmentally friendly bio-nanomaterials in EOR, and an even more limited understanding exists regarding the mechanisms by which biopolymer nanocomposites displace crude oil in porous media (Liu et al., 2024). Therefore, this study evaluated the successful synthesis of Ag NPs and the dispersibility and stability of E-Ag NPs through ultraviolet–visible spectroscopy (UV-Vis) spectroscopy, particle size analysis, Zeta potential measurement, X-ray powder crystal diffractometer (XRD), transmission electron microscopy (TEM), and scanning electron microscope (SEM). The interfacial activity of E-Ag NPs was assessed by IFT and contact angle measurements. Finally, through a series of oil recovery enhancement experiments, the synergistic potential and mechanisms of the biopolymer nanocomposites in improving oil recovery were comprehensively and systematically elucidated, providing new insights for the green and efficient development of oilfields.

2. Materials and methods

2.1. Materials

The strain used in the experiment was *Bacillus subtilis* isolated from crude oil that was extracted from the Yanchang Oilfield. NaCl, Na_2SO_4, $CaCl_2$, $MgCl_2$, $NaHCO_3$, $AgNO_3$, CH_3COOH, and NaOH were all analytically pure, Sinopharm Chemical Reagent Co. The oil used for the experiments was Changqing crude oil with a density of 0.867 g/cm^3 and a viscosity of 5.86 cP (25 °C). 20,000 mg/L mineralization brine: 0.133 g/L $NaSO_4$, 17.7868 g/L NaCl, 1.1431 g/L $CaCl_2$, 0.8640 g/L $MgCl_2$, 0.551 g/L $NaHCO_3$, 1 L deionized water.

2.2. EPS-mediated biosynthesis of Ag NPs with biopolymer nanocomposites established

Bacillus subtilis was inoculated and cultured in fermentation medium, at the end of which the fermentation broth was heated at 90 °C to inactivate the enzyme and centrifuged to remove the bacterium to obtain the polysaccharide-containing supernatant. The supernatant was mixed with anhydrous ethanol at a 1:3 vol ratio to precipitate crude polysaccharides. The crude polysaccharide precipitate was then dissolved in deionized water, and 80% trichloroacetic acid was added dropwise and centrifuged to remove the precipitated proteins, resulting in the final EPS solution. EPS was mixed with 20 mM/L Ag NO_3 at an EPS to Ag^+ volume ratio of 5:1. The pH of the mixed solution was adjusted to 9, and the reaction was allowed to continue at 60 °C for 24 h. A color change during the reaction indicated the generation of Ag NPs in the reaction mixture. At this point, the self-stabilized dispersion of Ag NPs in the EPS formed biopolymer nanocomposite fluids, which we refer to as E-Ag NPs. The experimental flow is shown in Fig. 1.

Fermentation medium: 5 g/L Tris, 6.5 g/L K_2HPO_4-$3H_2O$, 0.3 g/L KH_2PO_4, 1.5 g/L NH_4NO_3, 1.2 g/L succinic acid, 0.0001 g/L $CaSO_4$, 0.35 g/L K_2SO_4, 0.25 g/L $MgSO_4{\cdot}7H_2O$, and 10 mL/L chlorine-free trace element solution. Among the chlorine-free trace element solutions were 5.0 g/L $Na_2EDTA{\cdot}2H_2O$, 0.37 g/L Fe $(NO_3)_3{\cdot}9H_2O$, 0.05 g/L ZnO, 0.015 g/L $CuSO_4{\cdot}5H_2O$, 0.01 g/L $Co(NO_3)_2{\cdot}6H_2O$, 0.01 g/L $(NH_4)6Mo_7O_{24}{\cdot}4H_2O$ and 0.01 g/L H_3BO_3.

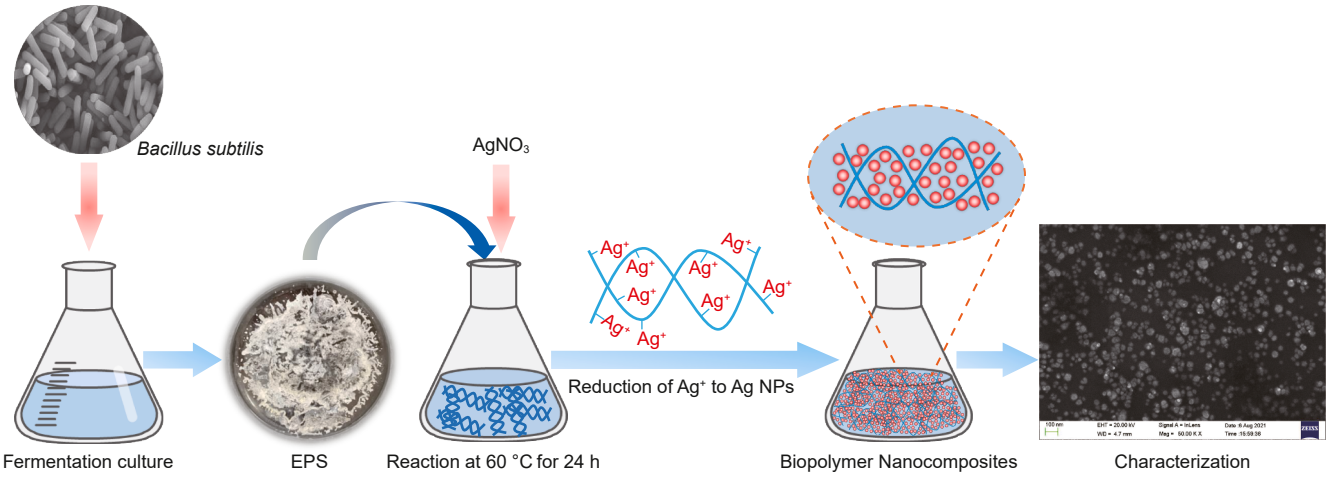

Fig. 1. Schematic diagram of the biosynthetic process for the preparation of biopolymer nanocomposite fluids E-Ag NPs.

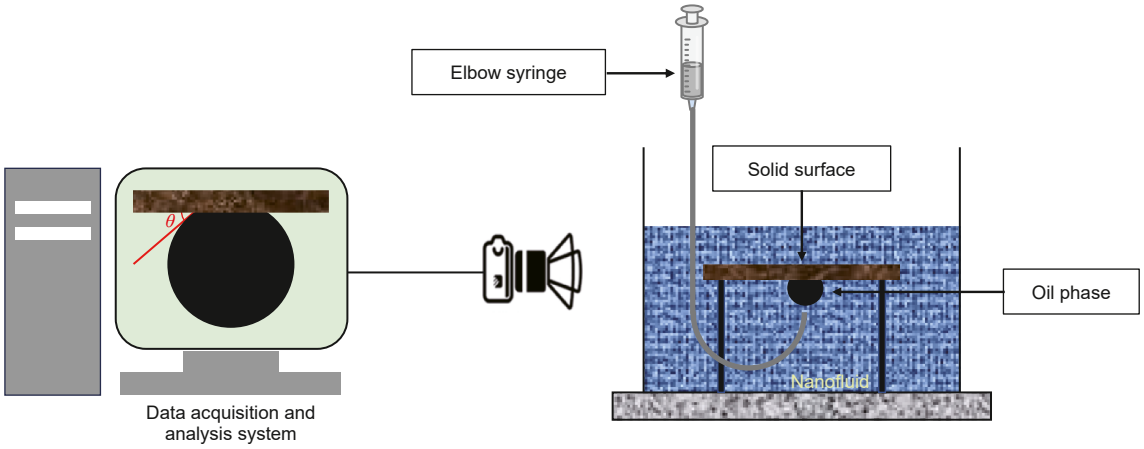

Fig. 2. Schematic diagram of contact angle measurement.

2.3. Characterization of biosynthesized Ag NPs

2.3.1. UV–Vis analysis

Absorption spectra of EPS-mediated synthesis of Ag NPs were scanned using a U-T6 UV spectrophotometer in the wavelength range of 300–800 nm at 5 nm intervals, and full-wavelength low-speed scans were performed to confirm the synthesis of Ag NPs.

2.3.2. Particle size distribution and Zeta potential analysis

Particle size distribution measurements of Ag NPs synthesized by EPS reduction were carried out by a Bettersize 2600 laser particle size distributor (wet method), in which water was used as the medium, with 1600 r of cycling and 3 min of sonication time.

The Zeta potential value of the solution was tested by Malvern laser particle sizer and the average value of three tests was taken as the experimental result. Where water was the medium, the dispersion dielectric constant was 78.5, the test temperature was 25.0 °C and the measurement position was 2.00 mm.

2.3.3. SEM and energy dispersive spectroscopy (EDS) analysis

A Zeiss SIGMA scanning electron microscope operating at 5.00–6.00 kV was used to observe the microscopic shape and size of the Ag NPs. The microscope was equipped with EDS to confirm the presence of the corresponding elements on the formed Ag NPs. Samples for SEM and EDS analysis were prepared by centrifuging at 4000 rpm for 20 min to obtain the NPs and washing them three times with 95% ethanol to remove soluble substances on the surface of the NPs. The samples were then freeze-dried in a vacuum freeze-drying to collect the lyophilized powdered samples. Finally, the samples were laid flat on conductive adhesive, coated with an ion sputtering apparatus, and placed into the electron microscope chamber for observation.

2.3.4. TEM analysis

The particles were dispersed with ethanol to remove particle agglomerates and then ultrasonicated for 10 min, then the samples were dropped onto a carbon coated copper grid and vacuum dried for 20 min before being placed under a JEM-2100Plus electron microscope to observe the microstructure and size.

2.3.5. FTIR analysis

The chemical composition of the EPS supernatant and E-Ag NPs was analyzed using a thermal infrared spectrometer (Thermo Scientific Nicolet 6700) at room temperature. The EPS and E-Ag NPs fluids were frozen into blocks in an ultra-low-temperature freezer at −80 °C, then transferred to a vacuum freeze dryer for freeze-drying, and the resulting powder was used for sampling. The samples were scanned 32 times in the range of 4000–400 cm^{-1} with a resolution of 4 cm^{-1}, and the functional

groups of EPS that might be involved in the synthesis reaction were analyzed based on the experimental results.

2.3.6. XRD analysis

The samples to be tested were freeze-dried to obtain powder samples, and the diffractograms were recorded using an X-ray diffractometer operating at 40 kV and 30 mA. The measurements were conducted for NPs in the 2θ range of diffraction angles from 10° to 90° with a scanning rate of 2°/s. The XRD analyses were carried out using Jade 6 software, and the obtained images were compared with a library of the Powder Diffraction Standards (JCPDS) to determine the crystal composition and structure.

2.3.7. Reservoir microbial toxicity assessment of NPs

The bacteria used in the experiment were *Bacillus* (Gram-positive) and *Pseudomonas aeruginosa* (Gram-negative), both of which are commonly found in reservoir and were isolated from oil–water samples collected from the Jianghan Oilfield in China. The bacteria were inoculated into Luria-Bertani (LB) medium and incubated at 37 °C until the exponential growth phase. The cells were then harvested by centrifugation and washed with a sodium chloride solution. Following protocols reported in previous studies on microbial toxicity assessment of NPs, the bacterial pellets were resuspended in solutions containing different concentrations of NPs (1, 5, and 10 mg/L), and incubated at the optimal growth temperature for 0, 12, 24, 36, and 48 h. The toxicity was assessed by calculating the number of colony-forming units (CFU) produced by the bacteria on agar plates (Fajardo et al., 2014). All treatments were performed in duplicate, and each experiment was repeated three times to ensure data reproducibility.

2.4. IFT measurement

The spin-drop method (Zhou et al., 2020) was used to test the IFT between crude oil and E-Ag NPs fluid. In this method, the oil phase forms long spherical or cylindrical droplets in the E-Ag NPs solution under the influence of three forces: centrifugal force, gravity, and interfacial tension. The IFT values were calculated by measuring the length, width, density difference, and rotational speed of the droplets in the two liquid phases. It is important to ensure that the length of the droplet along the rotation axis is between 4 and 6 times the droplet diameter to minimize errors caused by interfacial curvature. All measurements were repeated three times.

2.5. Evaluation of wettability

Wettability in a three-phase system is defined as oil-wetting for contact angles in the range of 105°–180°, neutral-wetting for angles in the range of 75°–105°, and water-wetting for angles in the range of 0°–75° (Treiber and Owens, 1972). To validate the ability of E-Ag NPs fluids to alter the wettability of reservoir rocks, the contact angle was measured using the hanging drop method with a DSA25 contact angle meter (KRUSS, Germany). The crude oil-aged core sample was placed into the sample chamber, and nanofluid was added to submerge the core piece. A 2 μL droplet of oil was then placed on the lower surface of the core piece using a bent-tube needle feeder. Measurement image analysis software was used to capture a photo and record the contact angle value (see Fig. 2).

2.6. Spontaneous imbibition

In low-permeability reservoirs, characteristics such as low porosity, low permeability, and small pore throat radius lead to significant capillary forces, resulting in imbibition effects. These factors influence both the production of crude oil and the degree of recovery in low-permeability fields. Experiments were conducted to evaluate the effect of spontaneous imbibition of E-Ag NPs fluids using the volumetric method. The cores were first placed in an airtight container and vacuumed for 24 h. They were then saturated using the evacuation-high-pressure method and aged for 2 weeks at 60 °C. After aging, the excess oil on the surface of the cores was wiped dry. The core was placed in an Amott imbibition flask, and nanofluid was added to raise the fluid to the graduated line. The imbibition unit was then placed in a high-temperature thermostat at 60 °C, and the amount of oil produced at various time intervals was recorded. The formula for imbibition recovery is as follows (Zhang et al., 2023):

$$E_m = \frac{V_{upper} - V_{lower}}{V_{oil}} \times 100\% \quad (1)$$

where E_m is the imbibition recovery rate; V_{upper} is the upper reading of the metering tube in mL; V_{lower} is the lower reading of the metering tube in mL; and V_{oil} is the saturated oil volume of the core in mL.

2.7. Nuclear magnetic resonance core flooding experiment

The experiment was carried out using a MacroMR12-150H NMR tester, with the magnet temperature controlled in the range of 31.99–32.01 °C, the resonance frequency of 8.5–12.8 MHz, and the magnet strength of 0.25 T ± 50 mT, which was used to reveal the strength and depth of the E-Ag NPs fluids and the Ag NPs fluid using the T_2 measurement method. The diagram of the experimental setup is shown in Fig. 3, and the main experimental steps are as follows: firstly, use the $MnCl_2$ solution with a mineralization of 50,000 ppm to drive off the distilled water in the core and carry out the NMR T_2 test, and observe whether the signal can be detected or not; next, inject the crude oil at 0.5 mL/min to build up the saturation degree of the bound water, saturate the crude oil, and carry out the NMR T_2 test, and observe the signal intensity; then inject the formation water at a constant rate of 0.5 mL/min at a constant rate to inject formation water, and inject oil displacement agent at the same rate. NMR T_2 tests were carried out throughout the exfoliation process to record the signal intensity at different stages, and real-time recordings were made of fluid production and pressure changes.

2.8. Microscopic flooding experiment

The glass micromodel, used as a porous medium, enables visualization of the nanofluid EOR mechanism at the pore scale, including the distribution and transport of nanofluids in the reservoir (Sharifipour et al., 2017). The glass micromodel used in the experiment had dimensions of 5 cm × 5 cm, a permeability of 20 μm^2, and a porosity of 22.14%. The micromodel was vacuumed and saturated with crude oil at a flow rate of 20 μL/min and then aged at room temperature for 12 h to ensure full contact between the crude oil and the inner wall of the micromodel. Brine flooding was performed by injecting brine at a rate of 0.05 mL/min until the oil content at the outlet was zero, after which the brine flooding was stopped to establish residual oil saturation. Nanofluid flooding was then carried out at the same injection rate, and the flooding was stopped when the oil content at the outlet was zero. The distribution of oil and water in the model after brine and nanofluid flooding was collected and recorded using a microscope throughout the experiment. Additionally, MATLAB software was

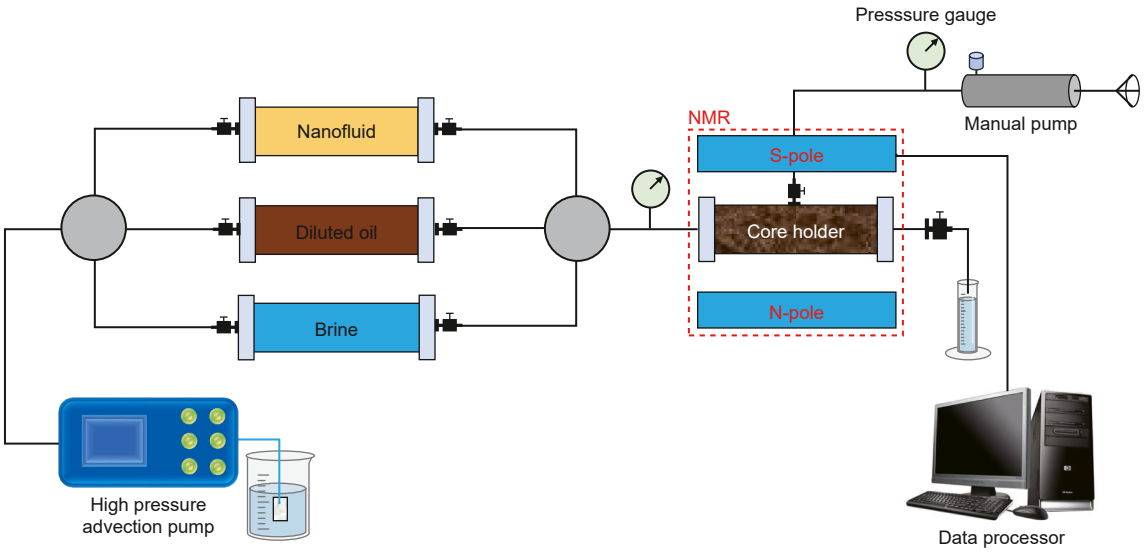

Fig. 3. Schematic diagram of the NMR core expulsion experiment.

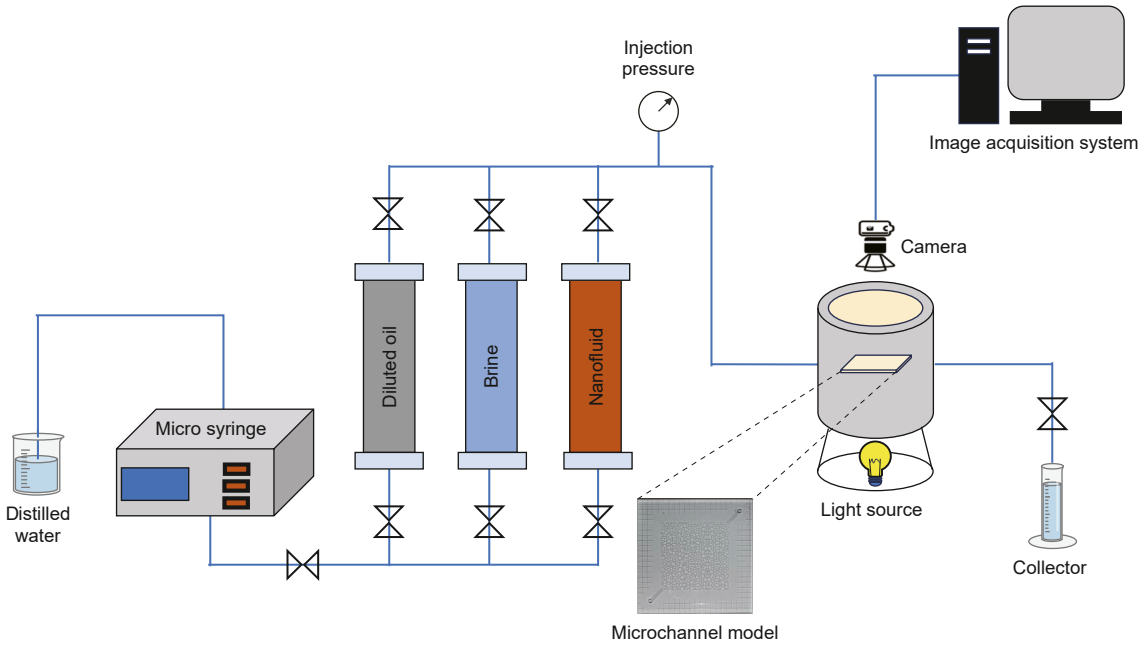

Fig. 4. Schematic diagram of microscopic flooding experiment.

employed to identify and process the flooded area and different types of residual oil (see Fig. 4).

3. Results and discussion

3.1. UV-Vis

The present study confirms the ability of EPS to reduce $AgNO_3$ to Ag NPs, as reported in other studies where the first indication of Ag NPs synthesis is a change in the solution color to brown (Veisi et al., 2018). As shown in Fig. 5(a), the color change of the solution from colorless to reddish-brown visually indicates the formation of Ag NPs, which is further confirmed by UV-Vis analysis. This color change is attributed to the interaction of electromagnetic fields generated by the collective oscillations of free conduction electrons excited by surface plasmon resonance (SPR) (Shanmuganathan et al., 2018; Subramaniam et al., 2022). The appearance of the SPR band in the 400–500 nm region is well-known as a typical indicator of Ag NPs formation (Djahaniani et al., 2017). After a certain reaction time, the mixed solution of EPS and $AgNO_3$ displayed a strong absorption peak in the wavelength range of 420 nm, confirming the synthesis of Ag NPs and indicating that the synthesized Ag NPs were stable. Therefore, the UV-Vis experimental results initially demonstrate the feasibility of using EPS for Ag NPs synthesis.

3.2. Particle size distribution

The results of the particle size distribution of Ag NPs are shown in Table 1. The average particle size of the synthesized Ag NPs was

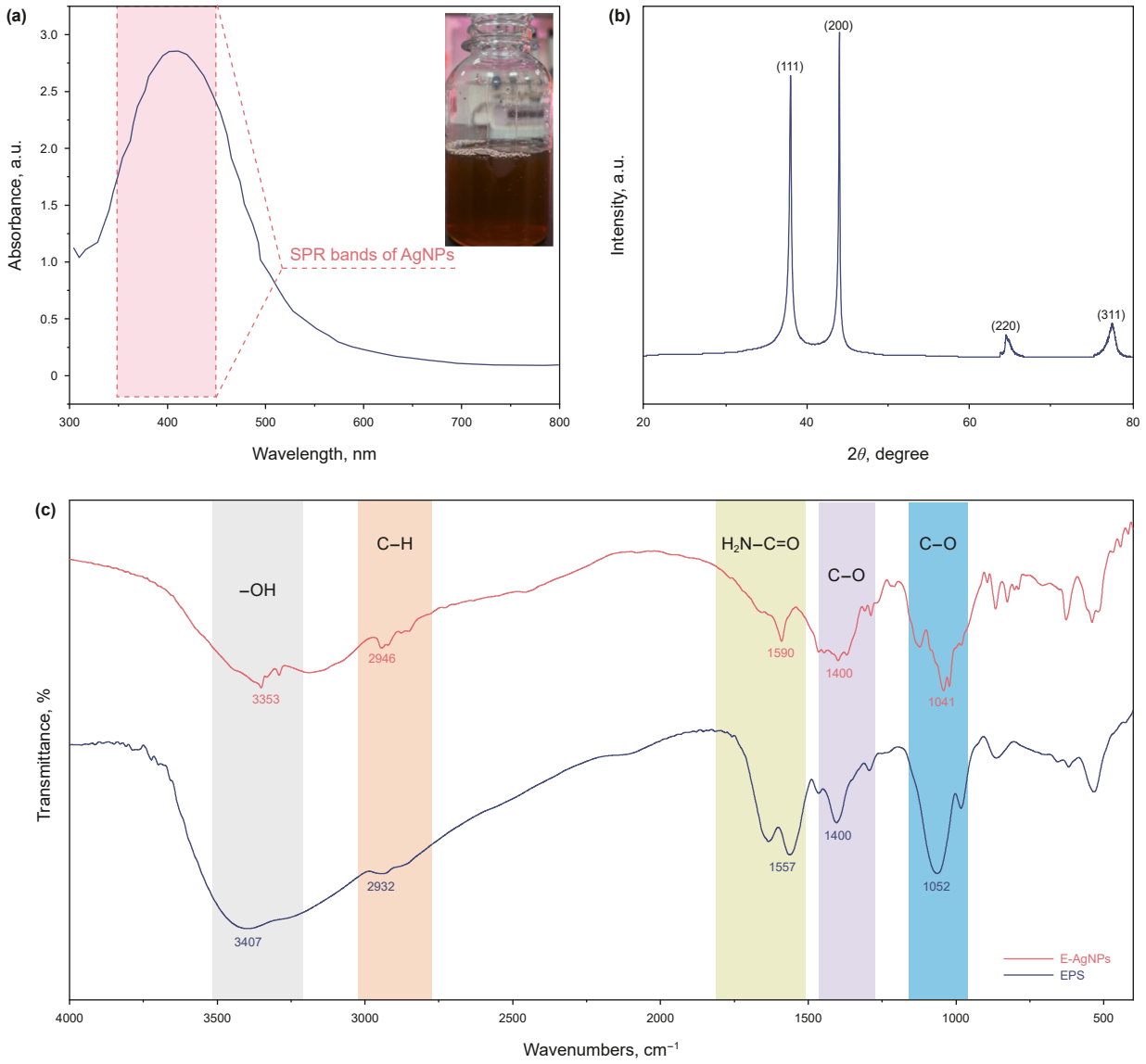

Fig. 5. **(a)** UV-Vis spectrogram of Ag NPs, **(b)** XRD pattern of Ag NPs, **(c)** FT-IR pattern of EPS and E-Ag NPs.

Table 1
Particle size distribution of Ag NPs synthesized by EPS.

Particle size, μm	Cum, %	Diff, %
0.000–0.020	0	0
0.020–0.050	83.99	83.99
0.050–0.100	97.44	13.45
0.100–0.150	97.47	0.03
0.150–0.200	97.85	0.38
0.200–0.250	98.68	0.82
0.250–0.300	99.54	0.86
0.350–0.400	99.8	0.27
0.400–0.450	99.97	0.17
0.450–0.500	100	0.03

experimentally measured to be 35 nm. NPs with a size ranging from 20 to 50 nm accounted for 83.99% of the total particle size, while 97.44% of the particles in the samples had a size of less than 100 nm. These results indicate that EPS is effective in reducing Ag^{+}, and the synthesized NPs are uniformly sized, homogeneous, and mono-dispersed.

3.3. FT-IR analysis

FT-IR analysis is a highly sensitive method for characterizing the formation of solid dispersions, capable of demonstrating structural alterations by shifting (or changing the intensity of absorption peaks in a molecule. Fig. 5(c) shows the FT-IR spectra of EPS and E-Ag NPs. In the spectrum of EPS, there is a broad peak at 3407 cm^{-1}, attributed to the presence of numerous hydroxyl groups and hydrogen bonds (–OH) in EPS. The peaks centered at 2932 and 1052 cm^{-1} correspond to the C–H stretching vibrations of the carbon chain and the C–O stretching vibrations of hydroxyl groups, respectively, which are commonly found in saccharides. The absorption peak at 1557 cm^{-1} is due to N–H bending and C–N stretching (class II amide), while the peak at 1400 cm^{-1} is attributed to the stretching vibration of C–O in the carboxyl group.

Whereas, in the spectra of E-Ag NPs, the formation of Ag NPs causes a slight shift in the peak at 3407 cm^{-1} and a decrease in its area, indicating that hydroxyl groups in the EPS structure are involved in the reduction and stabilization of Ag NPs. The peak at 1557 cm^{-1} also shifts slightly to the left and weakens, suggesting

an interaction between Ag^+ and the amide groups in EPS. Additionally, the peak at 1400 cm^{-1} weakens, indicating that carboxyl groups in EPS are also involved in the interaction (Veisi et al., 2018). The FT-IR spectator illustrates that EPS is rich in hydroxyl groups, which can specifically bind to precursor cations or monomers (Schnepp, 2013). This facilitates the reaction of Ag^+ with the polymer matrix, which is then reduced to metallic silver (Ag^0) upon heating. Subsequently, Ag^0 nucleates to form nuclei, which further aggregates to form Ag NPs that are then encapsulated and stabilized by EPS.

3.4. XRD analysis

The crystal structure properties of the EPS-mediated synthesis were investigated using X-ray diffraction (XRD) analysis. Four distinct diffraction peaks were recorded, determining the crystalline phase of the synthesized Ag NPs. As shown in Fig. 5(b), the XRD diffraction peaks of Ag NPs at 2θ values of 38.14°, 44.19°, 64.45°, and 77.40° correspond to the lattice planes (111), (200), (220), and (311). These results are consistent with the XRD results of synthesized Ag NPs reported in the relevant literature (Chinnathambi et al., 2023). All the characteristic diffraction peaks indicate that the synthesized Ag NPs possess a face-centered cubic (FCC) structure, which aligns with the standard values (JCPDS No. 04–0783) (Parthibavarman et al., 2019).

3.5. EDS analysis

The elemental composition of the samples was further analyzed by EDS energy spectroscopy, with the corresponding results shown in Fig. 6. EDS analysis confirmed the successful EPS-mediated synthesis of Ag NPs, revealing a strong characteristic peak of metallic Ag in the linear scan located at 3 keV (Lin et al., 2023). In a previous study, Vijayakumar et al. (2013) similarly confirmed the synthesis of Ag NPs in the range of 2–4 keV using Artemisia nilagirica. However, the results revealed the presence of a Si peak at approximately 1.74 keV, along with multiple escape peaks. This observation can be attributed to the low sample concentration deposited on a silicon substrate, where signal penetration or electron beam scattering from the underlying Si wafer introduced the Si peak. As shown in the bar chart in Fig. 6(a), the mass percentages of the elements C, O, and Ag are 13.33%, 21.84%, and 61.84%, respectively, with Ag having the highest mass percentage. The elemental mapping image in Fig. 6(b) further confirms the successful synthesis of Ag NPs through the obvious color contrast.

3.6. Stability analysis of E-Ag NPs

The Zeta potential, defined as the potential between the inner Helmholtz layer near the particle surface and the liquid in which the particle is suspended, represents the charge of the particle and indicates the potential stability of the colloidal system (Bahraminejad et al., 2024; Singh et al., 2014). Zeta potentials of NPs less than −30 mV or more than +30 mV suggest that the NPs are heavily positively or negatively charged, with repulsive forces dominating and thus stabilizing the system. Conversely, Zeta potentials between −30 mV and +30 mV indicate that the NPs are prone to aggregation and that the system is less stable (Ali et al., 2020; Sun et al., 2020). As shown in Fig. 7, the Zeta potential values of E-Ag NPs and Ag NPs are −43.4 and −28.2 mV, respectively. These results indicate that the surface of Ag NPs synthesized by EPS reduction is negatively charged and that E-Ag NPs formed by dispersion in EPS are better stabilized compared to a single Ag NPs fluid. Based on the DLVO theory (Peng et al., 2024; Sun et al., 2020), due to the presence of EPS, when NPs come into contact with EPS, the ions in the liquid are attracted to the surface of the NPs through van der Waals forces and electrostatic repulsion. This results in the formation of a dense ionic layer and a loose layer with opposite charges, known as the bilayer. The presence of this bilayer enhances the stability of the NPs in the liquid medium (Bukar et al., 2014; French et al., 2009). The high Zeta potential of

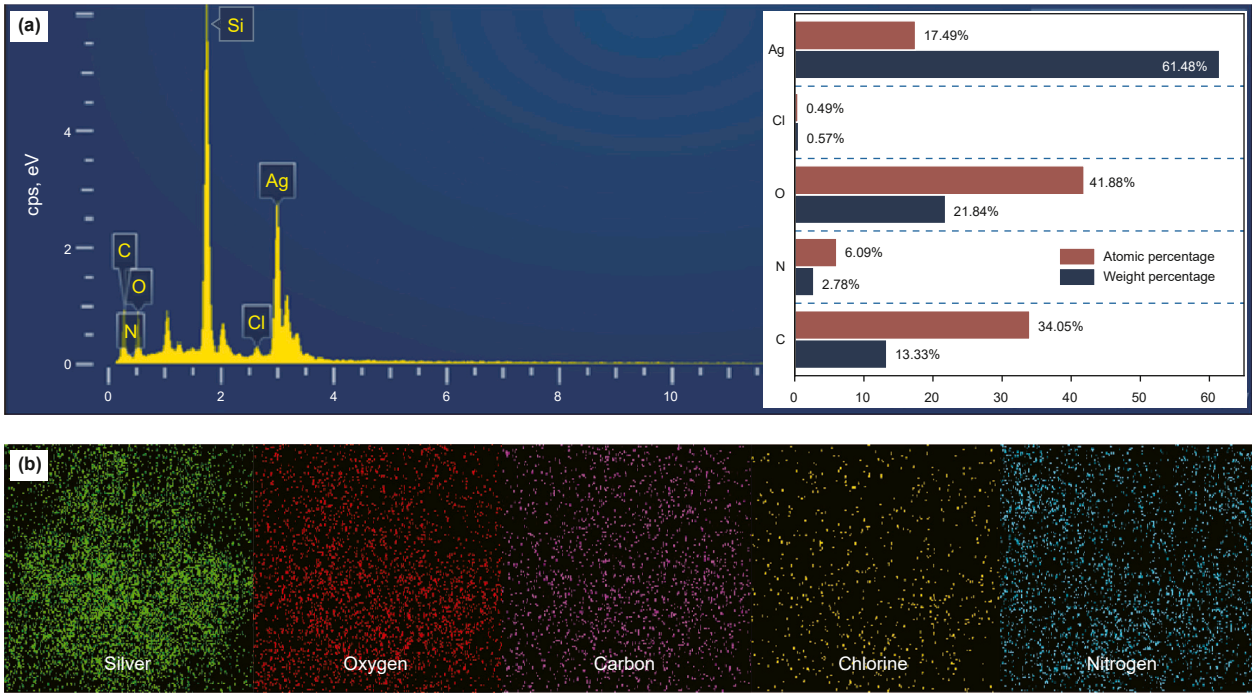

Fig. 6. EDS energy spectrum analysis profile of Ag NPs.

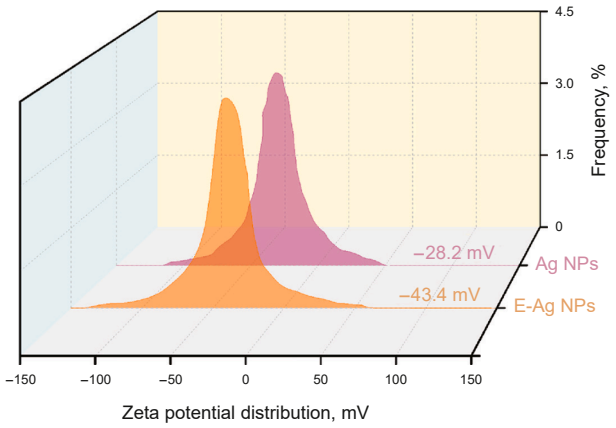

Fig. 7. Zeta potential analysis of E-Ag NPs and Ag NPs.

E-Ag NPs leads to stronger electrostatic repulsion between the NPs, which increases the difficulty of NPs agglomeration. Additionally, the hydrophilicity of the biopolymer EPS enhances the repulsion between ions in the outer layers of the particles, further contributing to the increased stability of the E-Ag NPs (Yakasai et al., 2021).

3.7. Dispersion analysis of E-Ag NPs

Transmission electron microscopy (TEM) and scanning electron microscopy (SEM) are evaluation methods used to measure particle size distribution and morphological features to describe the stability and dispersion of nanofluids (Chakraborty and Panigrahi, 2020). The experiments vividly demonstrated the size-morphology characteristics and dispersion of Ag NPs synthesized by EPS through SEM and TEM analyses (as shown in Fig. 8). The experimental results showed that Ag NPs dispersed without EPS appeared to be obviously agglomerated, as shown in Fig. 8(a) and (b), when the nanoparticles underwent a sedimentation mechanism, suggesting that the nanofluid at this point was unstable (Ali et al., 2018). In contrast, the dispersion of Ag NPs with EPS significantly improved the dispersion of the NPs, as shown in Fig. 8(c) and (d), with no obvious agglomeration of Ag NPs. The results in Fig. 8(c) show that the synthesized Ag NPs are mainly spherical, with sizes ranging from 20 to 50 nm, and have good dispersion. Fig. 8(d) TEM results show that Ag NPs are predominantly spherical and elliptical, but there are also irregular shapes such as polygons, with all particle sizes below 50 nm. The experimental results illustrate that EPS encapsulating Ag NPs can effectively inhibit the overgrowth of Ag NPs after nucleation and prevent the aggregation of NPs, thereby altering the dispersion properties of the nanofluid.

3.8. NPs toxicity analysis

The application of NPs in EOR is becoming increasingly widespread; however, their potential toxicity to the reservoir cannot be overlooked. Therefore, in this study, the microbial toxicity of NPs under reservoir conditions was preliminarily assessed by evaluating the effects of nanofluids on pure bacterial cultures at different exposure times and concentrations, as shown in Fig. 9. The experimental results showed that, compared to the control group, the bare Ag NPs exhibited a certain degree of toxicity toward both *Bacillus* and *Pseudomonas aeruginosa*. As shown in Fig. 9(a) and (b), a significant reduction in colony-forming units was observed after 12 h of exposure, and this effect became more

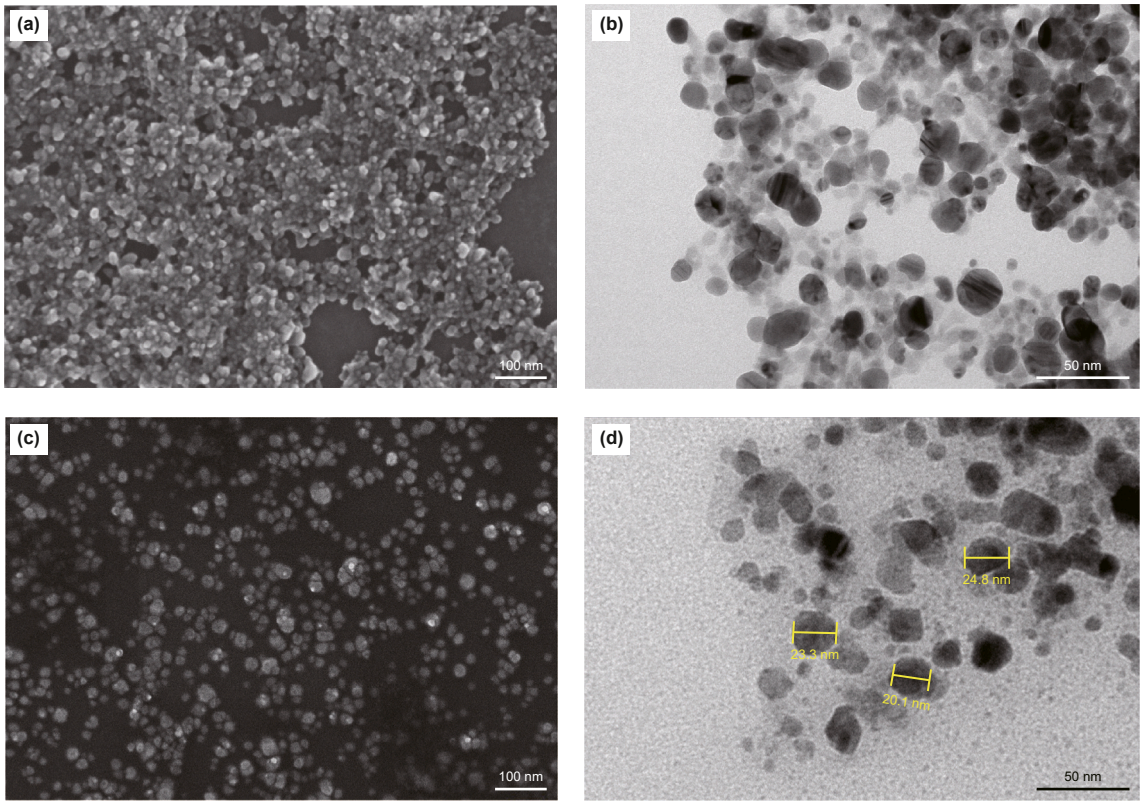

Fig. 8. **(a)** and **(b)** SEM and TEM patterns of Ag NPs without EPS dispersion, **(c)** and **(d)** SEM and TEM patterns of Ag NPs with EPS dispersion.

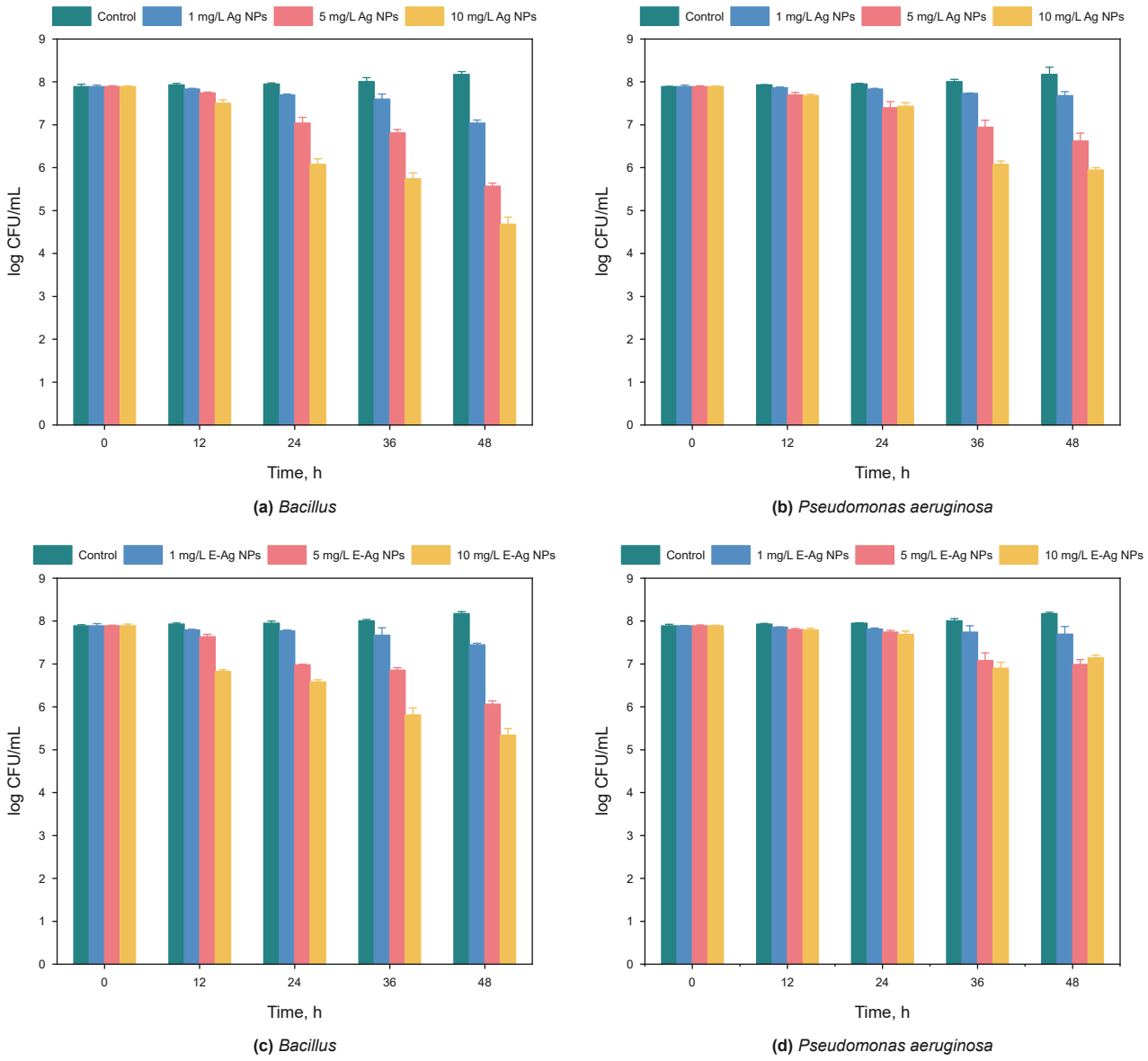

Fig. 9. Bar charts show the changes in colony-forming units of *Bacillus* and *Pseudomonas aeruginosa* strains. **(a)** *Bacillus* + Ag NPs, **(b)** *Pseudomonas aeruginosa* + Ag NPs, **(c)** *Bacillus* + E-Ag NPs, **(d)** *Pseudomonas aeruginosa* + E-Ag NPs.

pronounced with increasing NPs concentrations. In contrast, the E-Ag NPs significantly reduced the toxicity of bare Ag NPs, as shown in Fig. 9(c) and (d). Toxic effects on *Bacillus* and *Pseudomonas aeruginosa* were observed after 24 h of exposure, and the reduction in colony-forming units at various concentrations was notably less than that caused by bare Ag NPs. These findings suggest that the EPS-mediated synthesis and encapsulation of E-Ag NPs mitigated the toxicity of Ag NPs and enhanced their biocompatibility. As a result, E-Ag NPs can be considered a low-toxicity, highly biocompatible bionanofluid (Amooaghaie et al., 2015). Furthermore, EPS improved the dispersion stability of Ag NPs, reduced aggregation, and thereby also contributed to lower toxicity and enhanced biocompatibility (Thoms et al., 2024).

3.9. Analysis of the ability of E-Ag NPs to reduce IFT and alter wettability

IFT and wettability change are important factors in evaluating the EOR capability of nanocomposites (Manshad et al., 2024). Researchers have found that nanocomposites can reduce the IFT and contact angle between oil and water phases, and that there is an inverse relationship between IFT, contact angle, and nanofluid concentration (Omidi et al., 2020).

To verify the ability of E-Ag NPs to reduce IFT, experiments were conducted to measure the variation in IFT between E-Ag NPs and crude oil. The experimental results are shown in Fig. 10(a). The results indicate that the IFT value decreases gradually with the increase in the concentration of E-Ag NPs. A high concentration of E-Ag NPs can significantly reduce the oil-water interfacial tension. According to the calculations, the interfacial tension was 0.74 mN/m when the concentration of E-Ag NPs was 0 ppm. The oil-water interfacial tension reached its lowest point, 0.044 mN/m, when the concentration of E-Ag NPs increased to 1400 ppm, a reduction of 94.05%. Therefore, the change in the curves in the fig shows that the IFT decreases with the increase in NPs concentration, indicating that the IFT is highly sensitive to the nanofluid concentration.

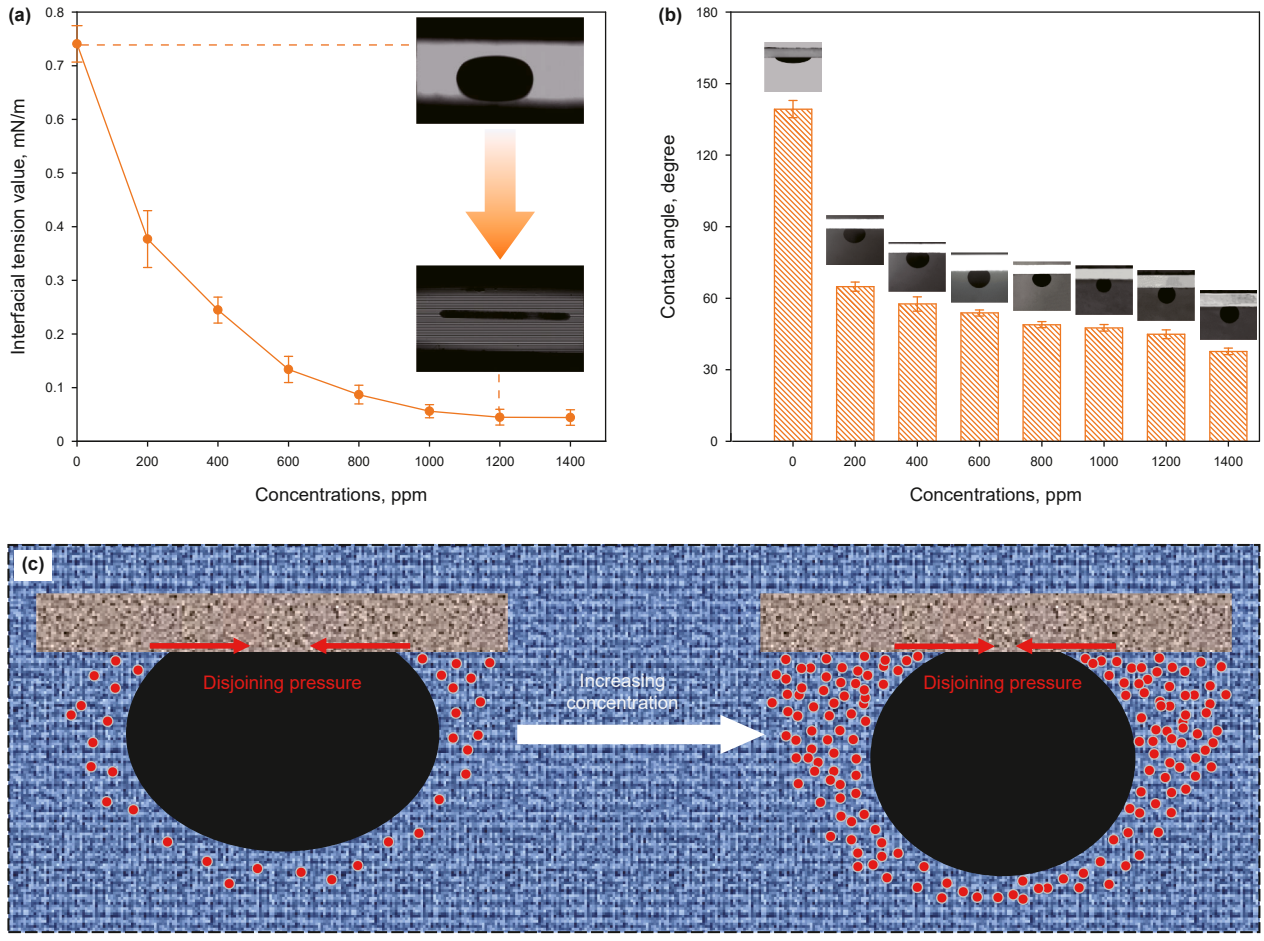

Fig. 10. **(a)** Variation of IFT of E-Ag NPs fluids at different concentrations, **(b)** variation of contact angle of E-Ag NPs fluids at different concentrations, **(c)** schematic diagram of change wettability.

Wettability alteration is a key factor in evaluating nanomaterials for EOR in porous media (Ahmadi et al., 2023; Bahraminejad et al., 2021). The study evaluated the ability of E-Ag NPs to alter wettability by measuring the change in the contact angle between crude oil and the core sample over a concentration range of 0–1400 ppm (Fig. 10(b)). The experimental results show that the contact angle is 144.3° when the concentration of E-Ag NPs is 0 ppm. The contact angle between the oil and solid phases decreases with the increase in the concentration of E-Ag NPs. When the concentration is increased to 1400 ppm, the contact angle decreases to a minimum of 37.7°. This indicates that E-Ag NPs can efficiently change the wettability of the rock surface from oil-wet to water-wet. As the concentration of E-Ag NPs increases, their ability to alter the rock surface wettability becomes stronger. As shown in Fig. 10(c), NPs dispersed at the junction of the three phases are arranged and accumulated in an ordered manner, forming a structural separation pressure (Dushkin et al., 1993; Nikolov and Wasan, 2009). As the number of NPs increases, their close stacking leads to an increase in structural separation pressure, which enhances the diffusion of nanoparticles on the solid surface (Bahraminejad et al., 2022; Wasan and Nikolov, 2003). This enhancement leads to a change in the wettability of the solid surface, manifested as a decrease in the contact angle (Wasan et al., 2011). A previous study has shown that the presence of EPS increases the dispersion stability of Ag NPs in liquid media. This increased dispersion stability allows E-Ag NPs to change wettability more efficiently (Ehtesabi et al., 2015).

3.10. Analysis of E-Ag NPs EOR performance

3.10.1. Spontaneous imbibition

The wetting phase is flooded by capillary forces into the pore throat channel to displace the non-wetting phase, a phenomenon known as imbibition. The experiment in which the displacement fluid displaces the crude oil in the core by capillary forces is known as the spontaneous imbibition oil experiment. This experiment can accurately and intuitively evaluate the effectiveness of nanofluid EOR. Fig. 11(a) and (b) depict the imbibition recovery and imbibition rate versus imbibition time of low-permeability cores under the influence of different E-Ag NPs concentrations, with the related experimental parameters shown in Table 2. The experimental results indicate that as the concentration of E-Ag NPs increases, both the imbibition recovery rate and the imbibition rate significantly increase. When the concentration of E-Ag NPs was 200 ppm, the imbibition recovery rate was 36.10%, and the imbibition rate was up to 3%/h. When the concentration of E-Ag NPs increased to 1000 ppm, the imbibition recovery rate increased to 54.89%, and the highest imbibition rate reached 15.8%/h. Correlation studies have shown that a high relative wettability index and a decrease in IFT enhance the efficiency of spontaneous imbibition of nanofluids (Guo et al., 2020; Wei et al., 2016). This means that the greater the change in wettability, the higher the imbibition recovery, and the lower the IFT, the faster the imbibition rate (Kathel and Mohanty, 2013; Sharma and Mohanty, 2013). Therefore, the higher the concentration of E-Ag NPs, the more effective

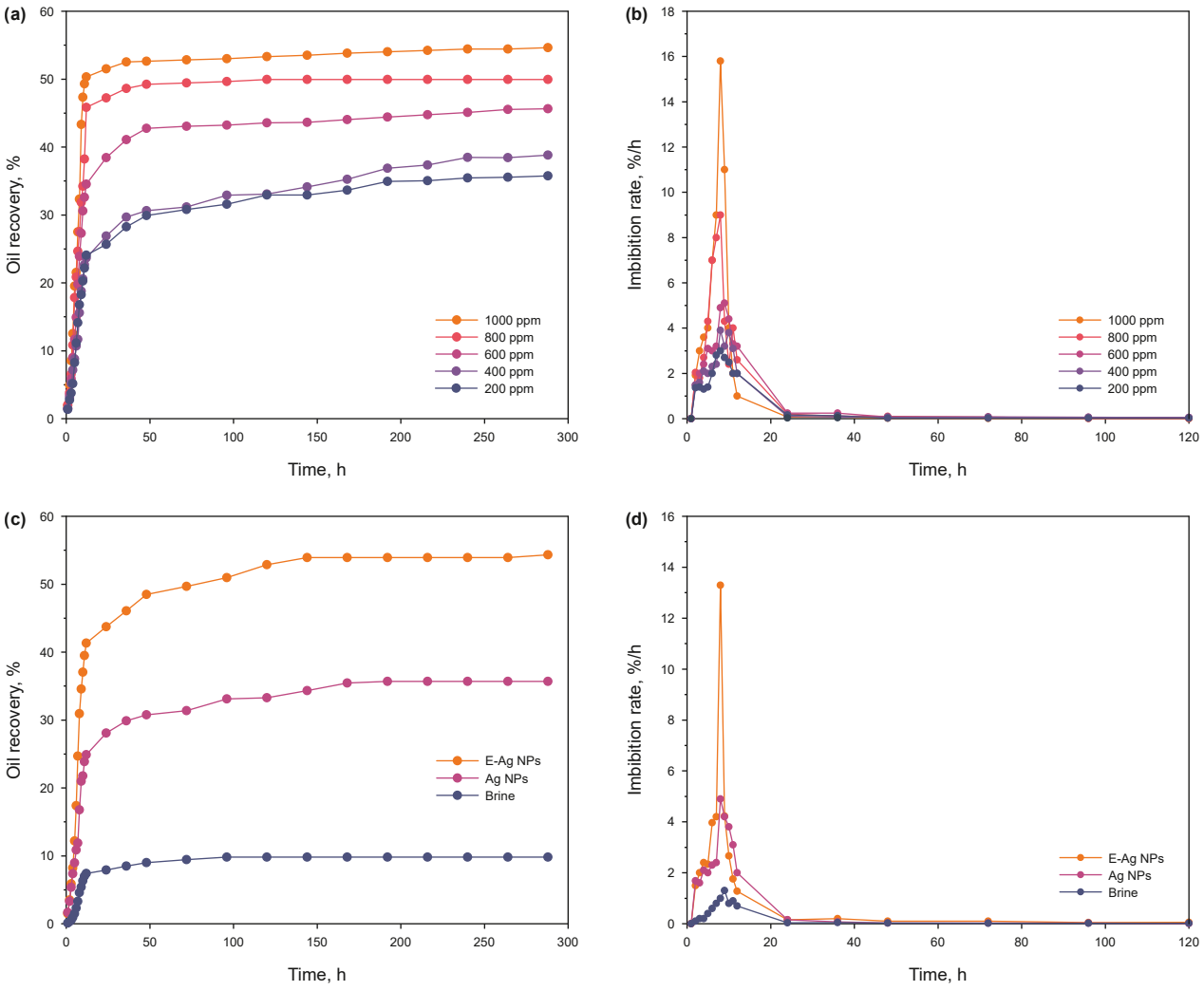

Fig. 11. Dynamic curve of spontaneous imbibition experiment. **(a)** Imbibition recovery at different concentrations, **(b)** imbibition rate at different concentrations, **(c)** imbibition recovery of different imbibition fluids, **(d)** imbibition rate of different imbibition fluids.

Table 2
Results of spontaneous imbibition experiments at different concentrations.

Core number	Concentration, ppm	Permeability, mD	Porosity, %	Oil saturation, %	Recovery rate, %
A1	200	1.83	13.16	68.79	36.10
A2	400	1.91	12.36	68.92	38.82
A3	600	1.95	13.23	69.64	45.65
A4	800	1.85	12.32	69.74	49.96
A5	1000	2.01	13.14	68.22	54.89

the wettability change and the reduces IFT, which explains the increase in imbibition recovery and imbibition rate with the increase in the concentration of E-Ag NPs.

In spontaneous imbibition experiments, the dispersion stability of NPs is also one of the key factors restricting the improvement of recovery efficiency (Ahmadi et al., 2023). As shown in Fig. 11(c), (d) and Table 3, at the same concentration, the spontaneous imbibition recovery efficiency of E-Ag NPs fluid is 54.32%, while that of Ag NPs fluid is only 35.68%. The spontaneous imbibition recovery efficiency and rate of E-Ag NPs are both higher than those of Ag NPs fluid. Rezaei et al. (2020) achieved a spontaneous imbibition oil recovery rate of 23% using cocamidopropyl betaine combined with SiO_2 nanoparticles, which represented a 14.7% increase in recovery compared to that using synthetic formation water alone (Rezaei et al., 2020). Sun et al. (2021) investigated a nonionic surfactant designed for tight oil-wet reservoirs, which was able to alter the core wettability from weakly oil-wet to weakly water-wet, achieving a spontaneous imbibition recovery rate of up to 35.61% (Sun et al., 2021). Zhao et al. (2018) prepared a silica nanofluid containing silica nanoparticles and surfactants and found that the spontaneous imbibition recovery of the surfactant alone was only 8%, whereas the silica nanofluid achieved a recovery of 16% (Zhao et al., 2018). In this study, the spontaneous imbibition recovery

Table 3
Results of spontaneous imbibition experiments with different imbibition liquids.

Core number	Imbibition fluid	Permeability, mD	Porosity, %	Oil saturation, %	Recovery rate, %
A6	E-Ag NPs	1.86	12.76	68.78	54.32
A7	Ag NPs	1.82	12.84	69.84	35.68
A8	Brine	1.95	13.02	69.88	9.8

Table 4
Results of core flooding experiments with different replacement fluids.

Core number	Displacement agent	Permeability, mD	Porosity, %	Oil saturation, %	Enhanced recovery rate, %	Final recovery rate, %
S1	E-Ag NPs	25.8	18.76	70.12	16.33	70.66
S2	Ag NPs	25.4	19.02	71.34	11.7	62.96

of the E-Ag NPs fluid reached 54.32%, indicating its remarkable EOR capability. On one hand, this is because the addition of EPS in E-Ag NPs fluid increases the viscosity of the fluid, reducing the viscosity ratio between the displacement fluid and the crude oil. Studies have found that the smaller the viscosity ratio between the displacement fluid and the crude oil, the better the spontaneous imbibition effect (Guo et al., 2020). On the other hand, the high dispersion stability of E-Ag NPs and the presence of EPS increase the number of NPs entering the porous medium, enhancing the wettability alteration effect. Therefore, this synergistically improves the spontaneous imbibition recovery efficiency of crude oil.

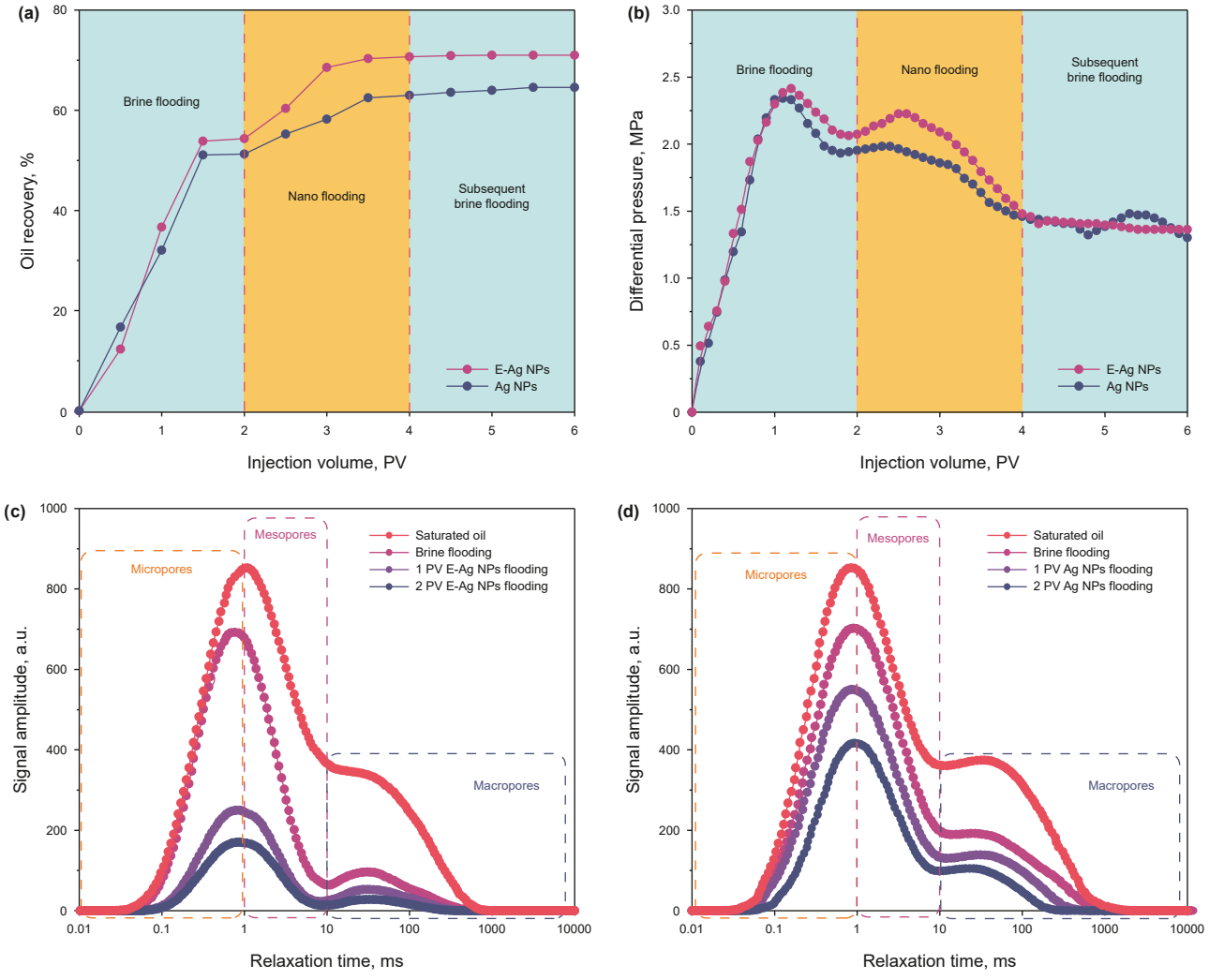

Fig. 12. Results of NMR core flooding experiments. **(a)** and **(b)** dynamic curves for enhanced recovery and pressure, **(c)** T_2 spectrum of E-Ag NPs nanofluids, **(d)** T_2 spectrum of Ag NPs fluids.

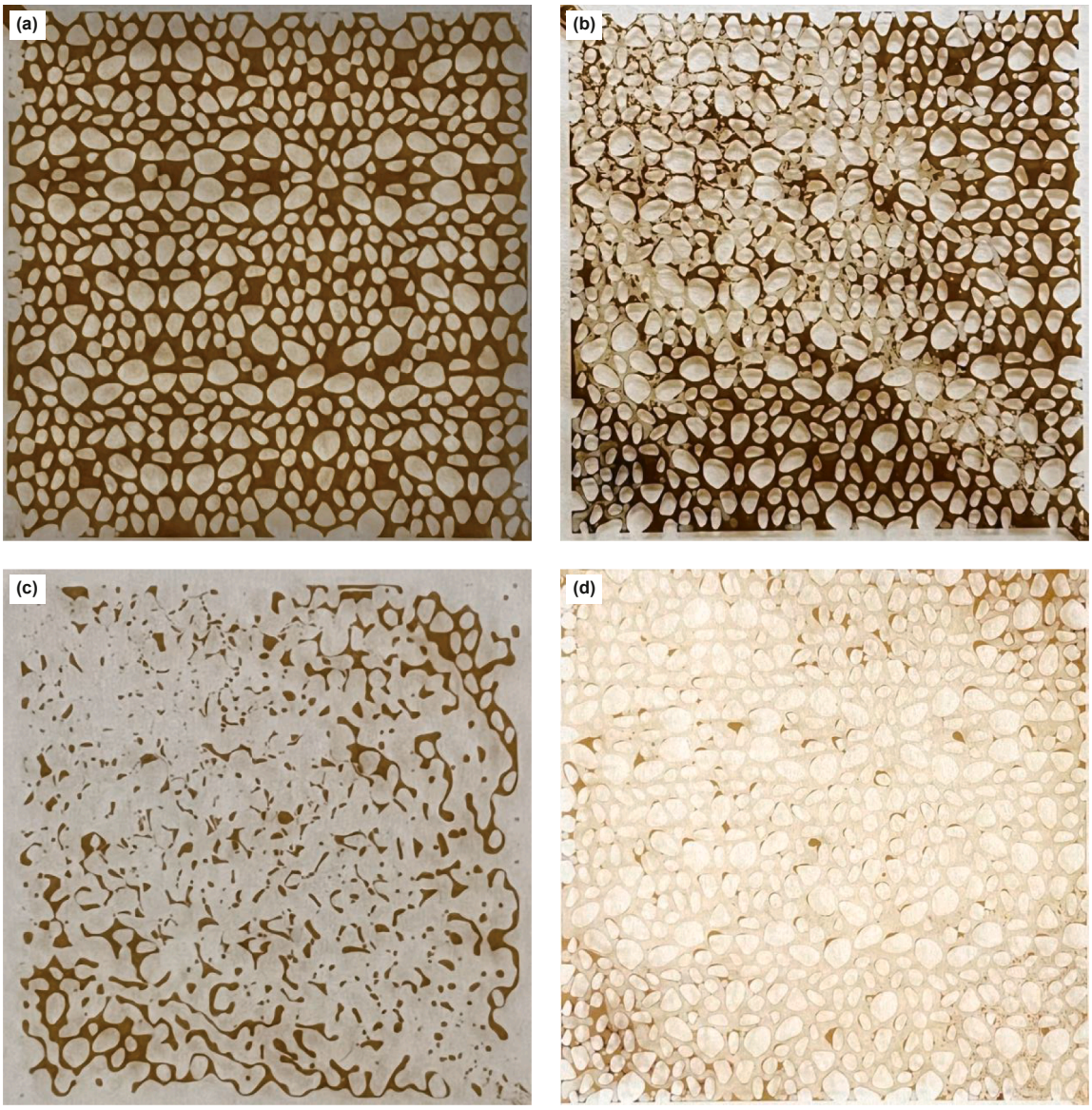

Fig. 13. **(a)** Glass model after saturated oil, **(b)** residual oil distribution after brine flooding, **(c)** residual oil distribution after Ag NPs fluid flooding, **(d)** residual oil distribution after E-Ag NPs fluid flooding.

3.10.2. Core flooding experiments and nuclear magnetic resonance analysis

Two low-permeability cores were selected for NMR core flooding experiments. The physical properties of the cores and the results of the displacement experiments are shown in Table 4. These results compare and analyze the synergistic EOR effect of EPS enhanced Ag NPs fluids and polymer nanocomposites for enhanced recovery. The recovery rate change curves and pressure drop curves are shown in Fig. 12(a) and (b). From these figures, we can see that the recovery rates during the primary brine flooding stage are 54.33% and 51.26%, respectively. During the displacement liquid flooding stage, the E-Ag NPs fluid increased crude oil recovery by 16.33%, while the Ag NPs fluid increased crude oil recovery by 11.7%. The experimental results clearly demonstrate that the E-Ag NPs fluid achieves more efficient EOR and can be considered a potential oil displacement. Similarly, according to the pressure drop curve analysis, the pressure drop of E-Ag NPs nanofluids is larger than that of Ag NPs fluids. Moreover, the pressure change of E-Ag NPs nanofluids is smaller than that of Ag NPs fluids during the subsequent brine flooding process. This implies that E-Ag NPs nanofluids can displace more residual oil than Ag NPs fluids in porous media. Therefore, the presence of EPS enhances the ability of Ag NPs fluid to improve recovery, and polymer nanocomposites exhibit superior enhanced recovery performance.

Fig. 12(c) and (d) shows the T_2 spectra of two cores with different displacement processes. The signal values of the NMR T_2 spectrum reflect the distribution characteristics of the remaining oil in different sizes of pores. Different relaxation times indicate different sizes of pores: those with relaxation times less than 1 ms are considered micropores, those with relaxation times from 1 to 10 ms are mesopores, and those with relaxation times greater than 10 ms are macropores (Liu et al., 2022; Zhang et al., 2024). Therefore, changes in the residual oil content of different pore sizes during the displacement process can be visualized based on the T_2 spectrum. From the T_2 spectrum in the saturated oil state, it can be seen that the signal peak is primarily distributed around 1 ms, indicating that the crude oil is mainly present in mesopores

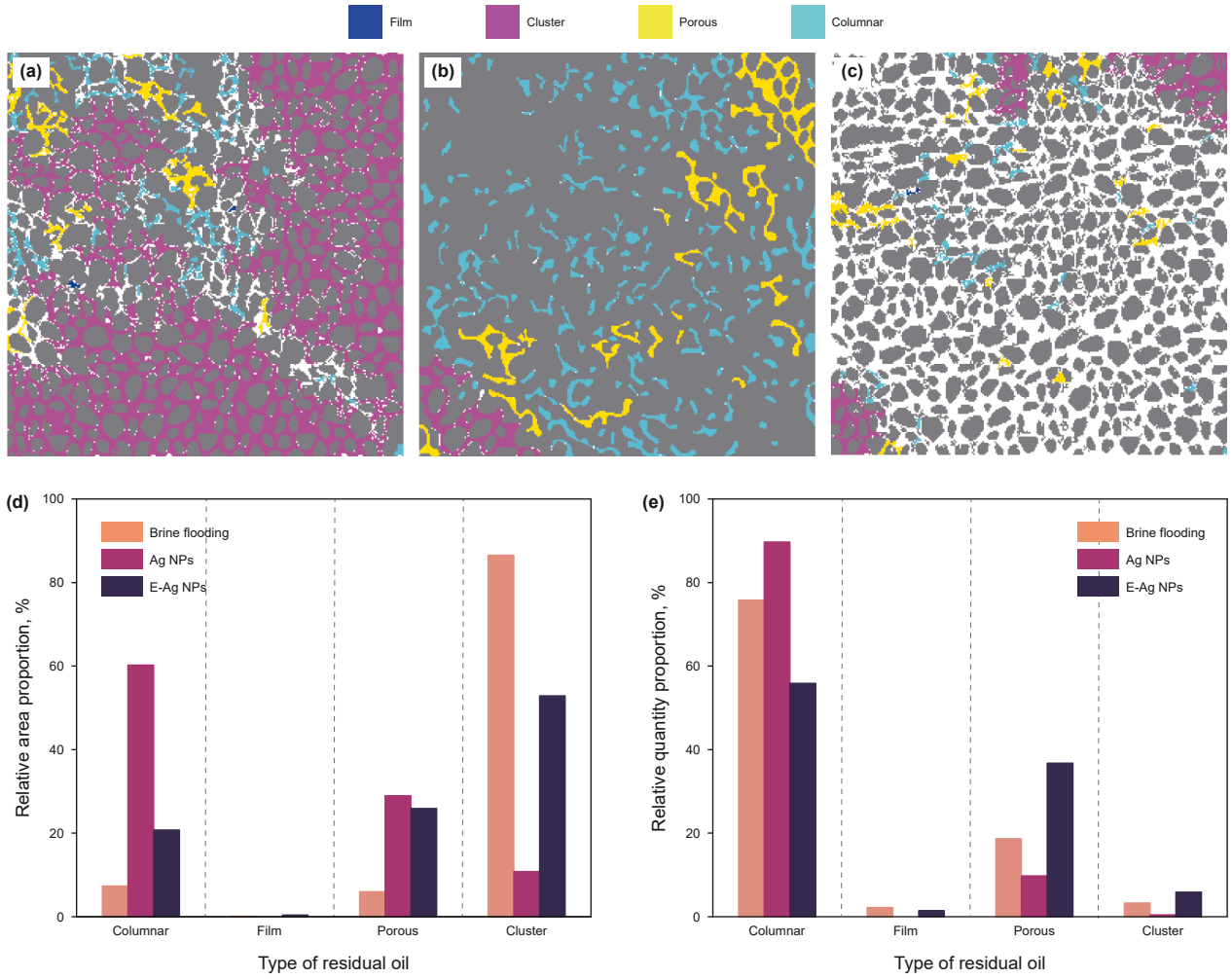

Fig. 14. **(a)** Schematic diagram of residual oil identification after brine flooding, **(b)** schematic diagram of residual oil identification after Ag NPs fluid flooding, **(c)** schematic diagram of residual oil identification after E-Ag NPs fluid flooding, **(d)** the percentage of the area of a single type of residual oil relative to the total area of all types of residual oil after brine flooding and nanofluid flooding, **(e)** the percentage of the quantity of a single type of residual oil relative to the total quantity of all types of residual oil after brine flooding and nanofluid flooding.

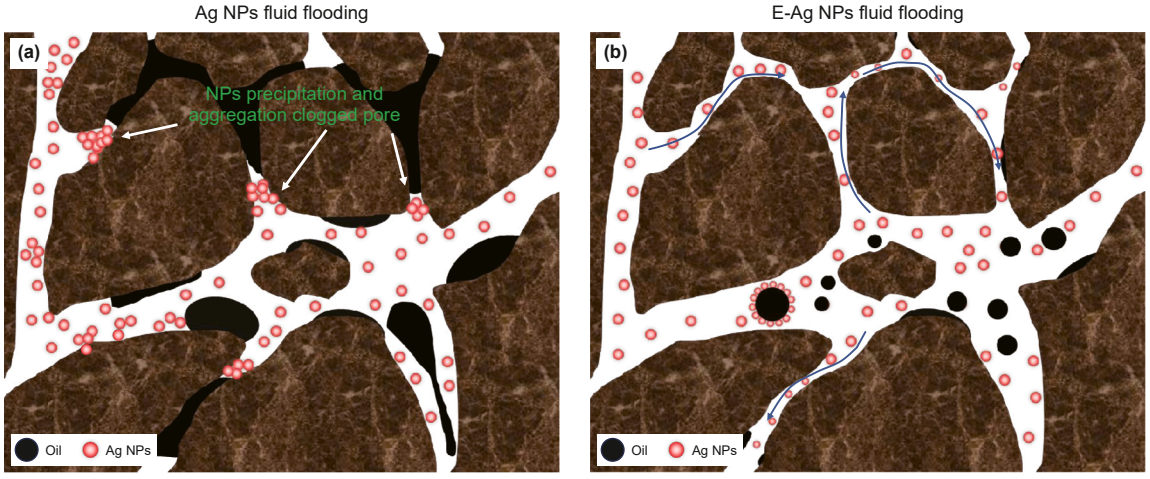

Fig. 15. Schematic diagram of EPS to reduce the aggregation and precipitation of Ag NPs versus enhancing the ability of Ag NPs to enter the low permeability area.

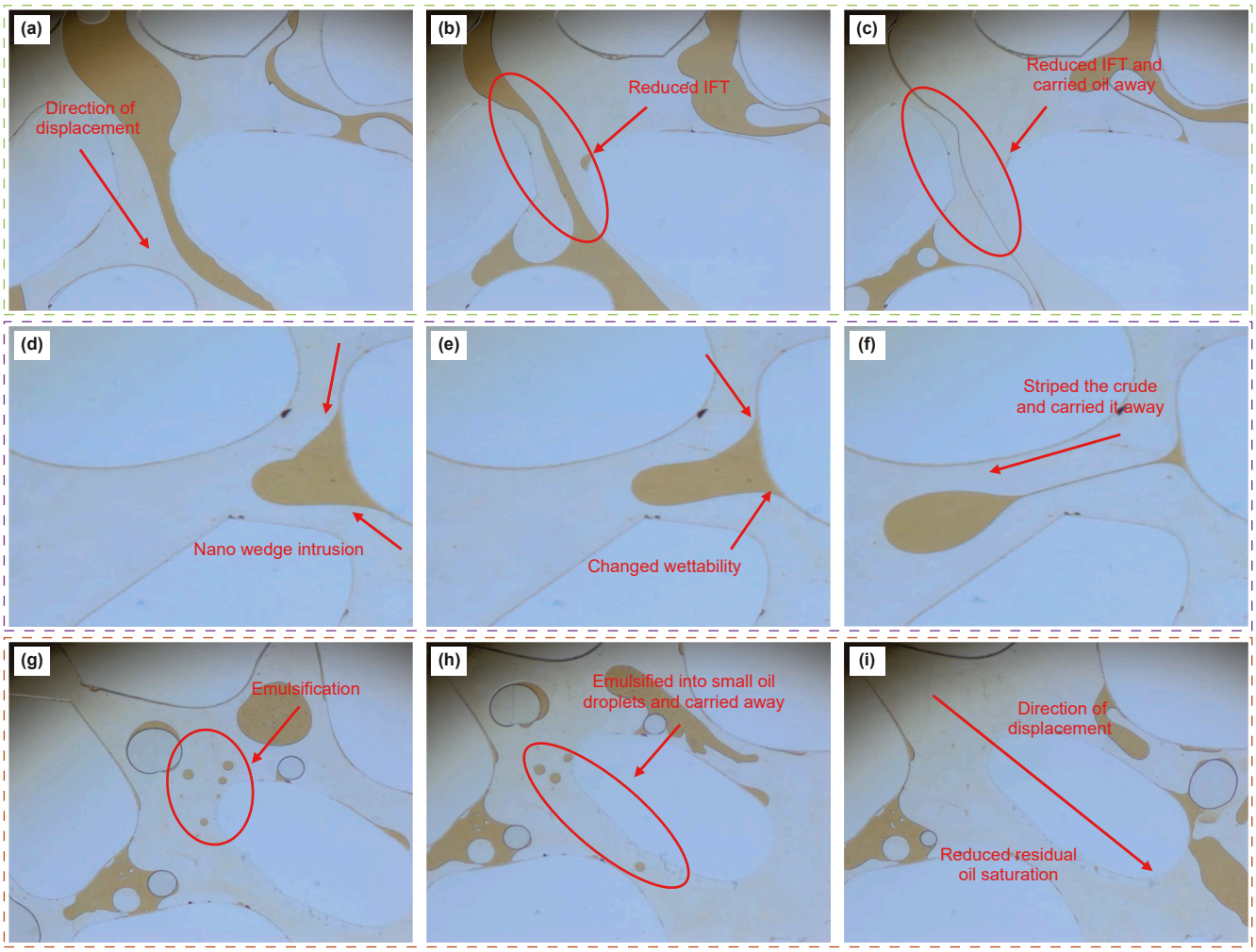

Fig. 16. Mechanisms of recovery enhancement by E-Ag NPs fluids. **(a)**–**(c)** reduction of IFT; **(d)**–**(f)** alteration of wettability; **(g)**–**(i)** emulsification.

and micropores. With the injection of brine flooding, the signal amplitude of the T_2 spectrum decreases gradually, but the reduced signal amplitude is mainly distributed in the macropores. Indicating that the brine flooding mainly displaces the crude oil that is easy to be displaced in the macropores in the core, and there is very little sweep in the mesopores and micropores.

The corresponding signal amplitudes of the T_2 spectrum were significantly reduced after flooding with both oil displacement agents. However, the signal amplitude of the T_2 spectrum decreases even more at around 1 ms after E-Ag NPs nanofluid flooding, and the signal value is almost zero after 10 ms. The peak position of the T_2 spectra shifted slightly to the right compared with that of water flooding, indicating that the E-Ag NPs nanofluid could displace more residual oil in the micropores and almost completely displace the residual oil in macropores. In contrast, Ag NPs fluid had limited ability to spread the residual oil in mesopores and micropores spaces. This is due to two main factors. First, EPS enhances the dispersion of Ag NPs, reduces the aggregation of Ag NPs, and improves the mobility ratio. The formation of a three-dimensional network structure by the bridging of EPS with Ag NPs enhances the fluidity of the nanofluid (El-hoshoudy, 2022; Kumar et al., 2017), allowing the NPs to enter smaller pore channels more effectively. Second, EPS enhances the stability of Ag NPs, and the increase in stability leads to a more efficient ability of E-Ag NPs nanofluids to change wettability and reduce IFT, which synergistically enhances recovery.

Moreover, we also found that the signal value of the T_2 spectrum of the residual oil after E-Ag NPs nanofluid flooding is much lower than that of Ag NPs fluid for the same flooding of 1 PV and two oil displacement agents. This also indicates that E-Ag NPs nanofluid is more efficient in enhancing recovery, and EPS enhances the effect of Ag NPs fluid in EOR.

3.10.3. *Microscopic flooding experiment*

The microscopic glass model can directly observe the distribution and transport of nanofluids in reservoir oil. Fig. 13(a) shows the glass model after being saturated with crude oil. It can be seen that the pore channels in the model are completely saturated with crude oil, and at this stage, the wettability of the glass channels within the model is oil-wet. Fig. 13(b) shows the distribution of residual oil after brine flooding. This primarily displaces the mobile and easily movable crude oil in the main flow lines of the channel, leaving a large amount of residual oil in the pore channels and resulting in an obvious fingering phenomenon. As shown in Fig. 13(c) and (d), after E-Ag NPs fluid and Ag NPs fluid flooding, both nanofluids improve sweep efficiency and residual oil recovery following brine flooding and reduce the occurrence of the fingering phenomenon. The generation and development of the

fingering phenomenon mainly depend on factors such as the mobility ratio, permeability, porosity, and heterogeneity (Kargozarfard et al., 2019). The viscosity of the displacement fluid can be increased, and the mobility ratio can be improved through the small-size effect of NPs with a high specific surface area, which enhances residual oil recovery.

Similarly, the experiment statistically analyzed the relative area and quantity distribution proportion of different types of residual oil after various fluid flooding, as shown in Fig. 14. The results indicated that after water flooding, most of the residual oil was in the cluster, porous, and columnar forms, with the relative area proportion of cluster residual oil being 86.52%, suggesting poor sweeping efficiency of residual oil during brine flooding. After Ag NPs fluid flooding, the proportion of cluster residual oil decreased, while the proportions of porous and columnar residual oil increased. This suggests that during the Ag NPs fluid flooding stage, cluster residual oil can be transformed into porous and columnar residual oil, indicating some efficiency. However, the displacement ability of Ag NPs fluid for different types of residual oil is limited. After E-Ag NPs fluid flooding, the area distribution of cluster, porous, and columnar residual oil significantly decreased. Compared to Ag NPs fluid flooding, the quantity of porous and columnar residual oil decreased substantially, demonstrating that E-Ag NPs fluid has high sweep efficiency and effective displacement performance (Dong et al., 2022).

Comparison reveals that although the wave area of Ag NPs fluid partially increases, there remains a significant amount of residual oil in the areas where the flow passes through, and the deeper residual oil at both ends of the channel is not displaced. In contrast, E-Ag NPs fluid significantly enhances sweep efficiency, opens the entire pore channel model, and displaces the residual oil almost completely. As shown in Fig. 15, compared to Ag NPs fluid, E-Ag NPs fluid improves the ability to open pore throat channels and reduces NPs aggregation or precipitation. On one hand, E-Ag NPs as polymer nanocomposites have a 3D network structure with viscoelastic behavior, which can displace residual oil in low-permeability zones through small-sized pores under certain displacement pressures (Pal and Mandal, 2020; Yue et al., 2018). On the other hand, according to Fig. 12(b), the pressure drop of E-Ag NPs fluid is larger, indicating that E-Ag NPs fluid has a higher drag coefficient and residual drag coefficient (Zhong et al., 2021). Therefore, E-Ag NPs fluid exhibits higher sweep efficiency, enabling it to penetrate and diffuse into more pore channels, displacing the deeper residual oil at both ends of the channel, thereby reducing residual oil saturation. Furthermore, we found that E-Ag NPs nanofluid, by reducing IFT, altering wettability, and emulsification during the displacement process, synergistically improves residual oil recovery, as shown in Fig. 16. The results of the microscopic displacement experiments and nuclear magnetic resonance core flooding experiments are consistent, further demonstrating the positive synergistic effect of E-Ag NPs nanofluid. This indicates its high efficiency in enhancing oil recovery, making it a promising new method for environmentally friendly and efficient crude oil recovery.

4. Conclusion

This study successfully developed a novel green and efficient biopolymer-based nanocomposite material that demonstrated significant effectiveness in EOR. Experimental results showed that E-Ag NPs exhibited excellent colloidal stability, with a Zeta potential absolute value 53.9% higher than that of Ag NPs solution. The NPs in the E-Ag NPs were well-dispersed, with an average particle size of approximately 35 nm. Moreover, the E-Ag NPs displayed high interfacial activity, achieving a minimum IFT of 0.044 mN/m and a minimum contact angle of 37.7°. In the EOR evaluation experiments, it was found that the spontaneous imbibition oil recovery reached 54.89% at an E-Ag NPs concentration of 1000 ppm. T_2 relaxation spectra revealed that after injecting 1 PV, E-Ag NPs effectively reduced the residual oil content in the porous medium, indicating a significant EOR effect. Furthermore, the experiments revealed that the primary EOR mechanisms of E-Ag NPs include the reduction of IFT, alteration of wettability, and emulsification of crude oil, which synergistically enhance the recovery of residual oil and significantly reduce the distribution of porous and columnar residual oil. Therefore, the biopolymer nanocomposite developed in this study provides a new approach for the green and efficient development of oilfields and sustainable development.

CRediT authorship contribution statement

Bo Wang: Writing – original draft, Methodology, Formal analysis, Conceptualization. **Shu-Yuan Deng:** Methodology, Formal analysis. **Hao Zeng:** Methodology, Formal analysis. **Feng-Peng Lai:** Methodology, Conceptualization. **Qing Feng:** Funding acquisition. **Xiao-Nan Li:** Supervision. **Yue-Hui She:** Writing – review & editing, Funding acquisition. **Fan Zhang:** Funding acquisition, Writing – review & editing.

Data availability

Data will be made available on request.

Declaration of competing interest

The authors declare no conflict of interest.

Acknowledgements

This study was supported by the National Natural Science Foundation of China in the form of grants awarded to FZ (52474053and 51774257) and YS (51574038 and 51634008).

References

Abbaspour, A., Jafari, A., Tarahomi, D.S., et al., 2023. Production and characterization of a polysaccharide/polyamide blend from Pseudomonas atacamensis M7D1 strain for enhanced oil recovery application. Int. J. Biol. Macromol. 240, 124421. https://doi.org/10.1016/j.ijbiomac.2023.124421.

Agi, A., Junin, R., Abbas, A., et al., 2020a. Effect of dynamic spreading and the disperse phase of crystalline starch nanoparticles in enhancing oil recovery at reservoir condition of a typical Sarawak oil field. Appl. Nanosci. 10, 263–279. https://doi.org/10.1007/s13204-019-01102-5.

Agi, A., Junin, R., Arsad, A., et al., 2020b. Ultrasound-assisted weak-acid hydrolysis of crystalline starch nanoparticles for chemical enhanced oil recovery. Int. J. Biol. Macromol. 148, 1251–1271. https://doi.org/10.1016/j.ijbiomac.2019.10.099.

Ahmadi, Y., Ayari, M.A., Olfati, M., et al., 2023. Application of green polymeric nanocomposites for enhanced oil recovery by spontaneous imbibition from carbonate reservoirs. Polym. Bull. (Berl.) 15 (14), 3064. https://doi.org/10.3390/polym15143064.

Ahmed, S., Ahmad, M., Swami, B.L., et al., 2016. A review on plants extract mediated synthesis of silver nanoparticles for antimicrobial applications: a green expertise. J. Adv. Res. 7 (1), 17–28. https://doi.org/10.1016/j.jare.2015.02.007.

Al-Anssari, S., Barifcani, A., Wang, S., et al., 2016. Wettability alteration of oil-wet carbonate by silica nanofluid. J. Colloid Interface Sci. 461, 435–442. https://doi.org/10.1016/j.jcis.2015.09.051.

Ali, J., Manshad, A.K., Imani, I., et al., 2020. Greenly synthesized magnetite@ SiO_2@ xanthan nanocomposites and its application in enhanced oil recovery: IFT reduction and wettability alteration. Arabian J. Sci. Eng. 45, 7751–7761. https://doi.org/10.1007/s13369-020-04377-x.

Ali, J.A., Kolo, K., Khaksar Manshad, A., et al., 2019. Modification of LoSal water performance in reducing interfacial tension using green ZnO/SiO_2 nanocomposite coated by xanthan. Appl. Nanosci. 9, 397–409. https://doi.org/10.1007/s13204-018-0923-5.

Ali, N., Teixeira, J.A., Addali, A., 2018. A review on nanofluids: fabrication, stability, and thermophysical properties. J. Nanomater. 2018, 1687–4110. https://doi.org/10.1155/2018/6978130.
Amooaghaie, R., Saeri, M.R., Azizi, M., 2015. Synthesis, characterization and biocompatibility of silver nanoparticles synthesized from Nigella sativa leaf extract in comparison with chemical silver nanoparticles. Ecotox Environ Safe 120, 400–408. https://doi.org/10.1016/j.ecoenv.2015.06.025.
Arsiya, F., Sayadi, M.H., Sobhani, S., 2017. Green synthesis of palladium nanoparticles using Chlorella vulgaris. Mater. Lett. 186, 113–115. https://doi.org/10.1016/j.matlet.2016.09.101.
Aziz, H., Tunio, S.Q., 2019. Enhancing oil recovery using nanoparticles—A review. Adv Nat Sci-Nanosci 10 (3), 033001. https://doi.org/10.1088/2043-6254/ab3bca.
Bahraminejad, H., Khaksar Manshad, A., Riazi, M., et al., 2019. CuO/TiO_2/PAM as a novel introduced hybrid agent for water—oil interfacial tension and wettability optimization in chemical enhanced oil recovery. Energy Fuel. 33 (11), 10547–10560. https://doi.org/10.1021/acs.energyfuels.9b02109.
Bahraminejad, H., Manshad, A.K., Iglauer, S., et al., 2022. NEOR mechanisms and performance analysis in carbonate/sandstone rock coated microfluidic systems. Fuel 309, 122327. https://doi.org/10.1016/j.fuel.2021.122327.
Bahraminejad, H., Manshad, A.K., Keshavarz, A., 2021. Characterization, micellization behavior, and performance of a novel surfactant derived from Gundelia tournefortii plant during chemical enhanced oil recovery. Energy Fuel. 35 (2), 1259–1272. https://doi.org/10.1021/acs.energyfuels.0c03272.
Bahraminejad, H., Manshad, A.K., Keshavarz, A., et al., 2024. Nanocomposite synergy for enhanced oil recovery: Macro and micro analysis of CeO_2/montmorillonite nanofluids in carbonate and sandstone reservoirs. Fuel 360, 130384. https://doi.org/10.1016/j.fuel.2023.130384.
Bajestani, M.I., Mousavi, S.M., Jafari, A., et al., 2017. Biosynthesis and physicochemical characterization of a bacterial polysaccharide/polyamide blend, applied for microfluidics study in porous media. Int. J. Biol. Macromol. 96, 100–110. https://doi.org/10.1016/j.ijbiomac.2016.11.048.
Becker, A., Vorhölter, F.J., Fjaervik, E., et al., 2009. Microbial Production of Biopolymers and Polymer Precursors. Xanthan Biosynthesis by Xanthomonas Bacteria: an Overview of the Current Biochemical and Genomic Data. Caister Academic Press, UK, pp. 1–13.
Bera, A., Belhaj, H., 2016. Application of nanotechnology by means of nanoparticles and nanodispersions in oil recovery-A comprehensive review. J. Nat. Gas Sci. Eng. 34, 1284–1309. https://doi.org/10.1016/j.jngse.2016.08.023.
Betancur, S., Giraldo, L.J., Carrasco-Marín, F., et al., 2019. Importance of the nanofluid preparation for ultra-low interfacial tension in enhanced oil recovery based on surfactant–nanoparticle–brine system interaction. ACS Omega 4 (14), 16171–16180. https://doi.org/10.1021/acsomega.9b02372.
Bukar, N., Zhao, S.S., Charbonneau, D.M., et al., 2014. Influence of the Debye length on the interaction of a small molecule-modified Au nanoparticle with a surface-bound bioreceptor. Chem. Commun. 50 (38), 4947–4950. https://doi.org/10.1039/c4cc01423e.
Chakraborty, S., Panigrahi, P.K., 2020. Stability of nanofluid: a review. Appl. Therm. Eng. 174, 115259. https://doi.org/10.1016/j.applthermaleng.2020.115259.
Chinnathambi, A., Alharbi, S.A., Joshi, D., et al., 2023. Synthesis of AgNPs from leaf extract of Naringi crenulata and evaluation of its antibacterial activity against multidrug resistant bacteria. Environ. Res. 216, 114455. https://doi.org/10.1016/j.envres.2022.114455.
Djahaniani, H., Rahimi-Nasrabadi, M., Saiedpour, M., et al., 2017. Facile synthesis of silver nanoparticles using Tribulus longipetalus extract and their antioxidant and antibacterial activities. Int. J. Food Prop. 20 (4), 922–930. https://doi.org/10.1080/10942912.2016.1188826.
Dong, L., Li, Y., Wen, J., et al., 2022. Functional characteristics and dominant enhanced oil recovery mechanism of polymeric surfactant. J. Mol. Liq. 354, 118921. https://doi.org/10.1016/j.molliq.2022.118921.
Druetta, P., Picchioni, F., 2019. Polymer and nanoparticles flooding as a new method for enhanced oil recovery. J. Petrol. Sci. Eng. 177, 479–495. https://doi.org/10.1016/j.petrol.2019.02.070.
Dushkin, C., Nagayama, K., Miwa, T., et al., 1993. Colored multilayers from transparent submicrometer spheres. Langmuir 9 (12), 3695–3701. https://doi.org/10.1021/la00036a055.
Dzhardimalieva, G., Bondarenko, L., Illés, E., et al., 2021. Colloidal stability of Silica-modified magnetite nanoparticles: comparison of various dispersion techniques. Nanomaterials-Basel. 11 (12). https://doi.org/10.3390/nano11123295, 3295.
Ehtesabi, H., Ahadian, M.M., Taghikhani, V., 2015. Enhanced heavy oil recovery using TiO_2 nanoparticles: investigation of deposition during transport in core plug. Energy Fuel. 29 (1), 1–8. https://doi.org/10.1021/ef5015605.
El-hoshoudy, A., 2022. Experimental and theoretical investigation for synthetic polymers, biopolymers and polymeric nanocomposites application in enhanced oil recovery operations. Arabian J. Sci. Eng. 47 (9), 1–29. https://doi.org/10.1007/s13369-021-06482-x.
Emadi, S., Shadizadeh, S.R., Manshad, A.K., et al., 2017. Effect of nano silica particles on Interfacial Tension (IFT) and mobility control of natural surfactant (Cedr Extraction) solution in enhanced oil recovery process by nano-surfactant flooding. J. Mol. Liq. 248, 163–167. https://doi.org/10.1016/j.molliq.2017.10.031.
Emam, H.E., Ahmed, H.B., 2016. Polysaccharides templates for assembly of nanosilver. Carbohyd polym 135, 300–307. https://doi.org/10.1016/j.carbpol.2015.08.095.
Esfe, M.H., Hosseinizadeh, E., Mosaferi, M., 2020. Investigation on nanofluid flooding effect on enhancement oil recovery process in a random pore distribution incomplete cone. Int Commun Heat Mass 117, 104629. https://doi.org/10.1016/j.icheatmasstransfer.2020.104629.
Fajardo, C., Saccà, M., Costa, G., et al., 2014. Impact of Ag and Al_2O_3 nanoparticles on soil organisms: in vitro and soil experiments. Sci. Total Environ. 473, 254–261. https://doi.org/10.1016/j.scitotenv.2013.12.043.
French, R.A., Jacobson, A.R., Kim, B., et al., 2009. Influence of ionic strength, pH, and cation valence on aggregation kinetics of titanium dioxide nanoparticles. Environ. Sci. Technol. 43 (5), 1354–1359. https://doi.org/10.1021/es802628n.
Gahlawat, G., Choudhury, A.R., 2019. A review on the biosynthesis of metal and metal salt nanoparticles by microbes. RSC Adv. 9 (23), 12944–12967. https://doi.org/10.1039/C8RA10483B.
Guo, J., Li, M., Chen, C., et al., 2020. Experimental investigation of spontaneous imbibition in tight sandstone reservoirs. J. Petrol. Sci. Eng. 193, 107395. https://doi.org/10.1016/j.petrol.2020.107395.
Hoseinzadeh, E., Makhdoumi, P., Taha, P., et al., 2017. A review on nano-antimicrobials: metal nanoparticles, methods and mechanisms. Curr. Drug Metabol. 18 (2), 120–128. https://doi.org/10.2174/1389200217666161201111146.
Iravani, M., Khalilnezhad, Z., Khalilnezhad, A., 2023. A review on application of nanoparticles for EOR purposes: history and current challenges. J. Pet. Explor. Prod. Technol. 13 (4), 959–994. https://doi.org/10.1007/s13202-022-01606-x.
Kargozarfard, Z., Riazi, M., Ayatollahi, S., 2019. Viscous fingering and its effect on areal sweep efficiency during waterflooding: an experimental study. Pet. Sci. 16, 105–116. https://doi.org/10.1007/s12182-018-0258-6.
Kathel, P., Mohanty, K.K., 2013. EOR in tight oil reservoirs through wettability alteration. In: Proceedings of SPE Annual Technical Conference and Exhibition. D021S0R08. https://doi.org/10.2118/166281-MS.
Kazemzadeh, Y., Sharifi, M., Riazi, M., 2018. Mutual effects of Fe_3O_4/chitosan nanocomposite and different ions in water for stability of water-in-oil (W/O) emulsions at low–high salinities. Energy Fuel. 32 (12), 12101–12117. https://doi.org/10.1021/acs.energyfuels.8b02449.
Kazemzadeh, Y., Shojaei, S., Riazi, M., et al., 2019. Review on application of nanoparticles for EOR purposes: a critical review of the opportunities and challenges. Chin. J. Chem. Eng. 27 (2), 237–246. https://doi.org/10.1016/j.cjche.2018.05.022.
Kumar, N., Gaur, T., Mandal, A., 2017. Characterization of SPN pickering emulsions for application in enhanced oil recovery. J. Ind. Eng. Chem. 54, 304–315. https://doi.org/10.1016/j.jiec.2017.06.005.
Lin, L., Wan, H., Mia, R., et al., 2023. Bioreduction and stabilization of antibacterial nanosilver using Radix Lithospermi phytonutrients for azo-contaminated wastewater treatment: synthesis, optimization and characterization. J. Cluster Sci. 34 (2), 1141–1155. https://doi.org/10.1007/s10876-022-02280-z.
Liu, Y.F., Dai, C.L., Zou, C.W., et al., 2022. Impact of flow rate on dynamic imbibition in fractured tight sandstone cores. Pet. Sci. 19 (6), 2895–2904. https://doi.org/10.1016/j.petsci.2022.07.007.
Liu, Y.L., Li, Y., Si, Y.F., et al., 2023. Synthesis of nanosilver particles mediated by microbial surfactants and its enhancement of crude oil recovery. Energy 272, 127123. https://doi.org/10.1016/j.energy.2023.127123.
Liu, Y., Fu, J., Zeng, H., et al., 2024. Synthesis of biological nanocomposite fluids and enhanced crude oil recovery. Fuel 363, 130954. https://doi.org/10.1016/j.fuel.2024.130954.
Malhotra, S.P.K., Alghuthaymi, M.A., 2022. Biomolecule-assisted biogenic synthesis of metallic nanoparticles. Agri-Waste. Microbes Product. Sustainable Nanomat. 139–163. https://doi.org/10.1016/B978-0-12-823575-1.00011-1.
Manshad, A.K., Mobaraki, M., Ali, J.A., et al., 2024. Biphasic interfacial functioning improvement using naturally derived Hop and dill surfactants in carbonate reservoirs. J. Environ. Chem. Eng. 12 (2), 112365. https://doi.org/10.1016/j.jece.2024.112365.
Maurya, N.K., Kushwaha, P., Mandal, A., 2017. Studies on interfacial and rheological properties of water soluble polymer grafted nanoparticle for application in enhanced oil recovery. J Taiwa Inst Chem E 70, 319–330. https://doi.org/10.1016/j.jtice.2016.10.021.
Maurya, N.K., Mandal, A., 2018. Investigation of synergistic effect of nanoparticle and surfactant in macro emulsion based EOR application in oil reservoirs. Chem. Eng. Res. Des. 132, 370–384. https://doi.org/10.1016/j.cherd.2018.01.049.
Morones, J.R., Elechiguerra, J.L., Camacho, A., et al., 2005. The bactericidal effect of silver nanoparticles. Nanotechnology 16 (10). https://doi.org/10.1088/0957-4484/16/10/059, 2346.
Nassar, N.N., Hassan, A., Pereira-Almao, P., 2011. Application of nanotechnology for heavy oil upgrading: catalytic steam gasification/cracking of asphaltenes. Energy Fuel. 25 (4), 1566–1570. https://doi.org/10.1021/ef2001772.
Nikolov, A.D., Wasan, D.T., 2009. Mechanisms of the assembly of nano-and microparticle two-dimensional structures in a wedge film. Ind. Eng. Chem. Res. 48 (5), 2320–2326. https://doi.org/10.1021/ie800934p.
Omidi, A., Manshad, A.K., Moradi, S., et al., 2020. Smart-and nano-hybrid chemical EOR flooding using Fe_3O_4/eggshell nanocomposites. J. Mol. Liq. 316, 113880. https://doi.org/10.1016/j.molliq.2020.113880.
Pal, N., Mandal, A., 2020. Enhanced oil recovery performance of gemini surfactant-stabilized nanoemulsions functionalized with partially hydrolyzed polymer/silica nanoparticles. Chem. Eng. Sci. 226, 115887. https://doi.org/10.1016/j.molliq.2020.113880.
Parthibavarman, M., Bhuvaneshwari, S., Jayashree, M., et al., 2019. Green synthesis of silver (Ag) nanoparticles using extract of apple and grape and with

enhanced visible light photocatalytic activity. BioNanoScience 9 (2), 423–432. https://doi.org/10.1007/s12668-019-0605-0.
Peng, B., Liao, P., Jiang, Y., 2024. A meta-analysis to revisit the property–aggregation relationships of carbon nanomaterials: experimental observations versus predictions of the DLVO theory. Langmuir 40 (13), 7127–7138. https://doi.org/10.1021/acs.langmuir.4c00274.
Rezaei, A., Riazi, M., Escrochi, M., et al., 2020. Integrating surfactant, alkali and nano-fluid flooding for enhanced oil recovery: a mechanistic experimental study of novel chemical combinations. J. Mol. Liq. 308, 113106. https://doi.org/10.1016/j.molliq.2020.113106.
Rezk, M.Y., Allam, N.K., 2019. Impact of nanotechnology on enhanced oil recovery: a mini-review. Ind. Eng. Chem. Res. 58 (36), 16287–16295. https://doi.org/10.1021/acs.iecr.9b03693.
Rezvani, H., Riazi, M., Tabaei, M., et al., 2018. Experimental investigation of interfacial properties in the EOR mechanisms by the novel synthesized Fe_3O_4@ Chitosan nanocomposites. Colloids Surf. 544, 15–27. https://doi.org/10.1016/j.colsurfa.2018.02.012.
Riaz, T., Iqbal, M.W., Jiang, B., et al., 2021. A review of the enzymatic, physical, and chemical modification techniques of xanthan gum. Int. J. Biol. Macromol. 186, 472–489. https://doi.org/10.1016/j.ijbiomac.2021.06.196.
Saravanan, A., Kumar, P.S., Karishma, S., et al., 2021. A review on biosynthesis of metal nanoparticles and its environmental applications. Chemosphere 264, 128580. https://doi.org/10.1016/j.chemosphere.2020.128580.
Schnepp, Z., 2013. Biopolymers as a flexible resource for nanochemistry. Angew. Chem. Int. Ed. 52 (4), 1096–1108. https://doi.org/10.1002/anie.201206943.
Shanmuganathan, R., MubarakAli, D., Prabakar, D., et al., 2018. An enhancement of antimicrobial efficacy of biogenic and ceftriaxone-conjugated silver nanoparticles: green approach. Environ. Sci. Pollut. Res. 25, 10362–10370. https://doi.org/10.1007/s11356-017-9367-9.
Sharifipour, M., Pourafshary, P., Nakhaee, A., 2017. Study of the effect of clay swelling on the oil recovery factor in porous media using a glass micromodel. Appl. Clay Sci. 141, 125–131. https://doi.org/10.1016/j.clay.2017.02.020.
Sharma, G., Mohanty, K.K., 2013. Wettability alteration in high-temperature and high-salinity carbonate reservoirs. SPE J. 18 (4), 646–655. https://doi.org/10.2118/147306-PA.
Sharma, T., Kumar, G.S., Chon, B.H., et al., 2015. Thermal stability of oil-in-water pickering emulsion in the presence of nanoparticle, surfactant, and polymer. J. Ind. Eng. Chem. 22, 324–334. https://doi.org/10.1016/j.jiec.2014.07.026.
Singh, S., Bharti, A., Meena, V.K., 2014. Structural, thermal, zeta potential and electrical properties of disaccharide reduced silver nanoparticles. J. Mater. Sci. Mater. Electron. 25, 3747–3752. https://doi.org/10.1007/s10854-014-2085-x.
Sofla, S.J.D., James, L.A., Zhang, Y., 2018. Insight into the stability of hydrophilic silica nanoparticles in seawater for enhanced oil recovery implications. Fuel 216, 559–571. https://doi.org/10.1016/j.fuel.2017.11.091.
Subramaniam, S., Kumarasamy, S., Narayanan, M., et al., 2022. Spectral and structure characterization of Ferula assafoetida fabricated silver nanoparticles and evaluation of its cytotoxic, and photocatalytic competence. Environ. Res. 204, 111987. https://doi.org/10.1016/j.envres.2021.111987.
Suleiman, M., 2019. Modelling and forecasting world oil demand: a regional analysis accounting for asymmetric price responses and technical progress. OPEC Energy Rev. 43 (2), 193–216. https://doi.org/10.1111/opec.12147.
Suleimanov, B.A., Abbasov, H.F., Ismayilov, R.H., 2023. Enhanced oil recovery with nanofluid injection. Petrol. Sci. Technol. 41 (18), 1734–1751. https://doi.org/10.1080/10916466.2022.2094959.
Sun, Y.P., Xin, Y., Lyu, F.T., et al., 2021. Experimental study on the mechanism of adsorption-improved imbibition in oil-wet tight sandstone by a nonionic surfactant for enhanced oil recovery. Pet. Sci. 18 (4), 1115–1126. https://doi.org/10.1016/j.petsci.2021.07.005.
Sun, Y., Yang, D., Shi, L., et al., 2020. Properties of nanofluids and their applications in enhanced oil recovery: a comprehensive review. Energy Fuel. 34 (2), 1202–1218. https://doi.org/10.1021/acs.energyfuels.9b03501.
Thoms, S., Gonsalves, R.A., Jos, e J., et al., 2024. Plant-based synthesis, characterization approaches, applications and toxicity of silver nanoparticles: a comprehensive review. J. Biotechnol. 394, 135–149. https://doi.org/10.1016/j.jbiotec.2024.08.009.
Treiber, L., Owens, W., 1972. A laboratory evaluation of the wettability of fifty oil-producing reservoirs. SPE J. 12 (6), 531–540. https://doi.org/10.2118/3526-PA.
Veisi, H., Azizi, S., Mohammadi, P., 2018. Green synthesis of the silver nanoparticles mediated by Thymbra spicata extract and its application as a heterogeneous and recyclable nanocatalyst for catalytic reduction of a variety of dyes in water. J. Clean. Prod. 170, 1536–1543. https://doi.org/10.1016/j.jclepro.2017.09.265.
Vijayakumar, M., Priya, K., Nancy, F., et al., 2013. Biosynthesis, characterisation and anti-bacterial effect of plant-mediated silver nanoparticles using Artemisia nilagirica. Ind. Crop. Prod. 41, 235–240. https://doi.org/10.1016/j.indcrop.2012.04.017.
Wang, S., Gu, Z., Guo, P., et al., 2024. Comparative laboratory wettability study of sandstone, tuff, and shale using 12-MHz NMR T_1-T_2 fluid typing: insight of shale. SPE J. 29 (9), 4781–4803. https://doi.org/10.2118/221496-PA.
Wasan, D., Nikolov, A., Kondiparty, K., 2011. The wetting and spreading of nanofluids on solids: role of the structural disjoining pressure. Curr Opin Colloid In 16 (4), 344–349. https://doi.org/10.1016/j.cocis.2011.02.001.
Wasan, D.T., Nikolov, A.D., 2003. Spreading of nanofluids on solids. Nature 423 (6936), 156–159. https://doi.org/10.1038/nature01591.
Wei, B., Qinzhi, L., Wang, Y., et al., 2018. An experimental study of enhanced oil recovery EOR using a green nano-suspension. In: Proceedings of SPE Improved Oil Recovery Conference. D051S27R02. https://doi.org/10.2118/190283-MS.
Wei, Q., Li, Z.P., Wang, X.Z., et al., 2016. Mechanism and influence factors of imbibition in fractured tight sandstone reservoir: an example from Chang8 reservoir of Wuqi area in Ordos basin. Petroleum Geology and Recovery Efficiency 23 (4), 102–107.
Yakasai, F., Jaafar, M.Z., Bandyopadhyay, S., et al., 2021. Current developments and future outlook in nanofluid flooding: a comprehensive review of various parameters influencing oil recovery mechanisms. J. Ind. Eng. Chem. 93, 138–162. https://doi.org/10.1016/j.jiec.2020.10.017.
Yue, M., Zhu, W., Han, H., et al., 2018. Experimental research on remaining oil distribution and recovery performances after nano-micron polymer particles injection by direct visualization. Fuel 212, 506–514. https://doi.org/10.1016/j.fuel.2017.10.055.
Zhang, C., Wen, H., Wang, X., et al., 2024. Formational stages of natural fractures revealed by U-Pb dating and CO-Sr-Nd isotopes of dolomites in the Ediacaran Dengying Formation, Sichuan Basin, southwest China. Geol. Soc. Am. Bull. 136 (11–12), 4671–4688. https://doi.org/10.1130/B37360.1.
Zhang, J., Huang, H., Zhang, M., et al., 2023. Experimental investigation of nanofluid enhanced oil recovery by spontaneous imbibition. RSC Adv. 13 (24), 16165–16174. https://doi.org/10.1039/d2ra06762e.
Zhao, M., Lv, W., Li, Y., et al., 2018. Study on the synergy between silica nanoparticles and surfactants for enhanced oil recovery during spontaneous imbibition. J. Mol. Liq. 261, 373–378. https://doi.org/10.1016/j.molliq.2018.04.034.
Zhong, X., Chen, J., An, R., et al., 2021. A state-of-the-art review of nanoparticle applications with a focus on heavy oil viscosity reduction. J. Mol. Liq. 344, 117845. https://doi.org/10.1016/j.molliq.2021.117845.
Zhou, Y., Wu, X., Zhong, X., et al., 2020. Development of silicon quantum dots based nano-fluid for enhanced oil recovery in tight Bakken cores. Fuel 277, 118203. https://doi.org/10.1016/j.fuel.2020.118203.